
Sketching Low-Rank Plus Diagonal Matrices

Andres Fernandez

Tübingen AI Center, University of Tübingen
a.fernandez@uni-tuebingen.de

Felix Dangel

Vector Institute, Toronto
fdangel@vectorinstitute.ai

Philipp Hennig

Tübingen AI Center, University of Tübingen
philipp.hennig@uni-tuebingen.de

Frank Schneider

Tübingen AI Center, University of Tübingen
f.schneider@uni-tuebingen.de

Abstract

Many relevant machine learning and scientific computing tasks involve high-dimensional linear operators accessible only via costly matrix-vector products. In this context, recent advances in sketched methods have enabled the construction of *either* low-rank *or* diagonal approximations from few matrix-vector products. This provides great speedup and scalability, but approximation errors arise due to the assumed simpler structure. This work introduces SKETCHLORD, a method that simultaneously estimates both low-rank *and* diagonal components, targeting the broader class of Low-Rank *plus* Diagonal (LoRD) linear operators. We demonstrate theoretically and empirically that this joint estimation is superior also to any sequential variant (diagonal-then-low-rank or low-rank-then-diagonal). Then, we cast SKETCHLORD as a convex optimization problem, leading to a scalable algorithm. Comprehensive experiments on synthetic (approximate) Low-Rank plus Diagonal (LoRD) matrices confirm SKETCHLORD’s performance in accurately recovering these structures. This positions it as a valuable addition to the structured approximation toolkit, particularly when high-fidelity approximations are desired for large-scale operators, such as the deep learning Hessian.

1 Introduction

High-dimensional linear operators are ubiquitous in modern data science, from the Hessian matrices of deep neural networks to large-scale scientific simulators. Due to their sheer size, these operators are often accessible only *implicitly* through their Matrix-Vector Products (MVPs). While MVP access suffices for many applications, we sometimes prefer an *explicit*, albeit possibly approximate, representation of the operator. Such an explicit approximate representation can be useful, e.g., for visualizations or compressing an operator that contains simpler sub-structures. To achieve this tractably, one typically resorts to structured approximations that are cheap to store and invert.

Recent advances in sketched methods enable the efficient construction of *either* Low-Rank (LoR) *or* Diagonal (D) approximations from a comparably small number of MVPs. However, these approaches can falter when the underlying linear operator exhibits a joint Low-Rank plus Diagonal (LoRD) structure, or can be well-approximated as such. Attempting to recover operators with such inherent or approximate LoRD structure using methods designed solely for either LoR or diagonal components leads to suboptimal results, even when applying them sequentially (Fig. 1 and Section 3).

To address this gap, we introduce SKETCHLORD, a novel sketched method designed for the *joint* recovery of both Low-Rank (LoR) *and* Diagonal (D) components simultaneously from a few MVPs of large-scale linear operators. **Our contributions are:**

- We analytically show that for LoRD operators, approximations for either Low-Rank (LoR) or Diagonal (D) components individually, or even sequentially (LoR-then-D or D-then-LoR), are inherently suboptimal (Section 3). We empirically verify this for sketched variants.
- As a solution, we propose SKETCHLORD, a joint approximation method that phrases the LoRD recovery as a convex optimization task, solvable efficiently via ADMM (Section 4). We provide practical accelerations, such as a new *compact recovery* strategy for any sketched methods.
- On synthetic matrices, we empirically show that SKETCHLORD achieves high-quality approximations across a broad class of (approximately) LoRD operators (Section 5). We also observe that SKETCHLORD is stable for a wide range of its hyperparameters (Section 4.2).

2 Background

Modern scientific computing and machine learning frequently encounter high-dimensional matrices, such as discretized differential operators in physical simulations or large covariance matrices. A prominent example motivating this work is the Hessian matrix in deep learning. Fundamental operations, like storing ($\mathcal{O}(N^2)$), performing explicit MVPs ($\mathcal{O}(N^2)$), or computing its inverse ($\mathcal{O}(N^3)$), become infeasible even for comparably modest neural networks parameter counts, N , in the millions. Implicit, matrix-free, MVPs—e.g., via Pearlmutter’s trick for the Hessian [Pearlmutter, 1994]—and structured approximations offer ways to nevertheless work with these massive matrices in practice. This work concentrates on achieving high-fidelity approximations for operators that are inherently Low-Rank plus Diagonal (LoRD) or can be accurately represented by such a structure.

Structured approximations. To render large operators tractable, various structured approximations are employed in practice. Low-rank captures dominant modes while diagonal approximations simplify interactions to element-wise scaling. Another instance, K-FAC [Martens and Grosse, 2015], a popular Hessian approximation, employs a Kronecker-factored block-diagonal structure, primarily for computational efficiency in optimization. Crucially, the “best” approximation strategy is determined not only by the operator’s intrinsic structure but also by a critical trade-off: the application’s demand for *approximation quality* (low approximation error) versus constraints on the acceptable *runtime* and available *memory*. In essence, the specific application dictates whether a fast-but-coarse approximation suffices or if a potentially slower but more accurate representation is desired, and how memory constraints influence this choice. In this paper, we focus on the composite Low-Rank plus Diagonal (LoRD) structure. Evidence suggests that important and complex operators, such as the Hessian matrix in deep learning, may be well-approximated by such a structure. For example, spectral analyses show dominant low-rank components [e.g. Sagun et al., 2018, Popyan, 2018, Ghorbani et al., 2019], while common practices like diagonal regularizers introducing a diagonal contribution. Developing robust methods for high-quality LoRD approximation is thus of significant practical interest.

Sketched methods for structured recovery. Sketched methods, based on random matrix theory, offer a data-efficient paradigm for constructing these structured approximations from only a limited number, p , of MVP measurements. Due to their scalability, reliability, and ability to be parallelized [Halko et al., 2011], they have steadily gained popularity in many applications including signal processing [Couillet and Debbah, 2013], scientific computing [Li et al., 2014, Tropp et al., 2019], or machine learning [Dereziński and Mahoney, 2024, Fernandez et al., 2025]. Here, we focus on sketched methods for low-rank and diagonal recovery. Sketched methods like XDIAG [Epperly et al., 2024] or DIAG++ are based on the Girard-Hutchinson estimator and allow estimating $\text{diag}(\mathbf{A})$ from only $p \ll k =: \text{rank}(\mathbf{A})$ random measurements. In this work, we compare to XDIAG which exhibits improved measurement-efficiency. Similarly, a Sketched Singular Value Decomposition (SSVD) provides an approximate SVD of a low-rank operator, using p left and right measurements, followed by QR orthogonalization, and an SVD of size $p \times p$ (see Alg. 3). Crucially, using p slightly larger than k is enough with high probability [Halko et al., 2011, Tropp et al., 2017]. When \mathbf{A} is not truly low-rank, an oversampled recovery mechanism can be used instead to reduce noise [Boutsidis et al., 2016, Tropp et al., 2019].

Joint recovery with rank minimization. Consider the following general problem of rank minimization under linear mapping \mathcal{M} as e.g. studied in Candès and Tao [2010]:

$$(P_0) \quad \mathbf{X}_{\natural} = \arg \min_{\mathbf{X}} \text{rank}(\mathbf{X}) \quad \text{s.t.} \quad \mathcal{M}(\mathbf{X}) = \mathbf{M} \quad (1)$$

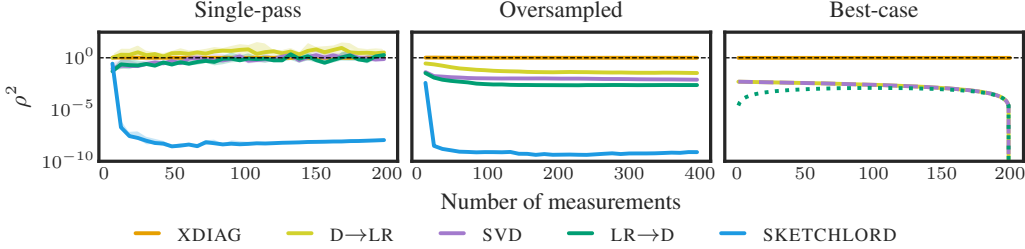


Figure 1: **Joint recovery is superior for the Low-Rank plus Diagonal (LoRD) operator $\mathbf{A} = \mathbf{1}\mathbf{1}^\top + \mathbf{I}$:** (Left & Center) Empirical recovery performance of various sketched Low-Rank (LoR) and Diagonal (D) approximation methods versus number of measurements, using single-pass or oversampled recovery. SKETCHLORD’s joint recovery of the LoR and D component consistently yields superior approximations compared to individual or sequential recovery strategies. Medians (thick lines) and interquartile ranges (shaded region, 25th-75th percentiles, 30 samples) are shown. For reference, the dashed line marks 100% relative error (ρ^2), below which methods outperform an all-zero recovery. (Right) Theoretical best-case recovery error bounds for different LoR/D recoveries, as derived in Section 3. SKETCHLORD is omitted due to its zero theoretical error.

Though NP-hard in general [Natarajan, 1995], its convex relaxation is equivalent with high probability when \mathcal{M} is sufficiently random and yields enough measurements [Candès and Tao, 2010]:

$$(P_1 \equiv P_0) \quad \mathbf{X}_{\natural} = \arg \min_{\mathbf{X}} \|\mathbf{X}\|_* \quad \text{s.t.} \quad \mathcal{M}(\mathbf{X}) = \mathbf{M} \quad (2)$$

This objective, in turn, admits a Lagrangian characterization that is equivalent for some $\lambda \in \mathbb{R}_{\geq 0}$:¹

$$(P_\lambda \equiv P_1) \quad \mathbf{X}_{\natural} = \arg \min_{\mathbf{X}} \frac{1}{2} \underbrace{\|\mathbf{M} - \mathcal{M}(\mathbf{X})\|_F^2}_{\mathcal{L}_2} + \lambda \|\mathbf{X}\|_* \quad (3)$$

To solve it efficiently, Cai et al. [2010] proposed to use an instance of ADMM [Boyd et al., 2011], that in its simplest form, runs the following *projected gradient* step iteratively (for step size $\eta \in \mathbb{R}_{>0}$):

$$\mathbf{X} \leftarrow \mathcal{P}_\lambda(\mathbf{X} - \eta \nabla_{\mathbf{X}} \mathcal{L}_2) \quad (4)$$

where \mathcal{P}_λ is the *spectral shrinkage* operator, computed by applying a soft threshold to the singular values of its input (optimality is discussed in [Cai et al., 2010, Th.2.1]).

3 The need for joint recovery

To illustrate the necessity for *joint* Low-Rank plus Diagonal (LoRD) recovery, we consider a canonical instance of this operator class, $\mathbf{A} := \mathbf{1}\mathbf{1}^\top + \mathbf{I} \in \mathbb{R}^{N \times N}$ with $N \gg 1$. This operator, while simple, encapsulates the core challenge: its structure is an explicit sum of a rank-1 component ($\mathbf{1}\mathbf{1}^\top$) and a full-rank diagonal component (\mathbf{I}). In this section, we first demonstrate that attempting to recover this structure through separate or sequential approximations is fundamentally suboptimal (Section 3.1). After that, we empirically verify these findings (Section 3.2) by applying sketched versions of these strategies to \mathbf{A} (with $N = 200$). To measure the recovery error of an approximation $\hat{\mathbf{X}}$ for a linear operator \mathbf{X} , we use the *residual energy* (lower is better) defined as:

$$\rho_{\hat{\mathbf{X}}}^2(\mathbf{X}) := \frac{\|\mathbf{X} - \hat{\mathbf{X}}\|_F^2}{\|\mathbf{X}\|_F^2} \in \mathbb{R}_{\geq 0}. \quad (5)$$

3.1 Theoretical analysis

Diagonal approximation. Approximating \mathbf{A} by its diagonal, $\hat{\mathbf{A}} = \text{diag}(\mathbf{A}) = 2\mathbf{I}$, the error is:

$$\rho_{\mathbf{D}}^2(\mathbf{A}) = \frac{\|\mathbf{A} - \text{diag}(\mathbf{A})\|_F^2}{\|\mathbf{A}\|_F^2} = \frac{N^2 - N}{N^2 + 3N} = \frac{N - 1}{N + 3}, \quad (6)$$

¹Analytical λ is unavailable, with a few exceptions [e.g. Candès et al., 2011, Tomioka and Suzuki, 2010].

i.e. *purely diagonal approximations reach near worst-case error already for moderate N .*

Low-rank approximation. To analize the rank- k optimal approximation: $\hat{\mathbf{A}} = \llbracket \mathbf{A} \rrbracket_k = \sum_{i=0}^{k-1} \lambda_i \mathbf{v}_i \mathbf{v}_i^\top$, with eigenvectors \mathbf{v}_i and eigenvalues λ_i , we observe that \mathbf{A} is a Toeplitz matrix, and thus admits the following eigendecomposition: $\mathbf{A} = \mathbf{F}^{-1}(N \cdot \mathbf{e}_0 \mathbf{e}_0^\top + \mathbf{I}) \mathbf{F}$, where \mathbf{F} is the discrete Fourier basis of corresponding dimension and \mathbf{e}_i is the standard basis vector with nonzero value at the (zero-indexed) i -th position. We can then express the ρ -optimal rank- k approximation analytically as: $\llbracket \mathbf{A} \rrbracket_k := N \cdot \mathbf{f}_0 \mathbf{f}_0^* + \sum_{i=0}^{k-1} \mathbf{f}_i \mathbf{f}_i^*$ and the error for the resulting optimal rank- k deflation becomes

$$\rho_{\text{LoR}}^2(\mathbf{A}) = \frac{N - k}{N^2 + 3N} = \frac{1 - k/N}{N + 3} \in \left[0, \frac{1 - 1/N}{N + 3}\right].$$

This is drastically better than a diagonal approximation due to the dominance of the \mathbf{f}_0 component. For an operator of the shape $\mathbf{I} + \sigma \mathbf{1} \mathbf{1}^\top$ and $\sigma \ll 1$, this approximation would not be that favorable. Furthermore, this approximation entails a poor tradeoff for all $k \geq 2$, since each additional eigenpair only improves the error by a small fraction, and a zero-error approximation requires $k = N$.

Diagonal-then-low-rank. This sequential approximation, first extracts the diagonal and then applies a low-rank approximation to the residual, i.e. $\hat{\mathbf{A}} = \text{diag}(\mathbf{A}) + \llbracket \mathbf{A} - \text{diag}(\mathbf{A}) \rrbracket_k$. The residual $\bar{\mathbf{A}} := \mathbf{A} - \text{diag}(\mathbf{A}) = \mathbf{F}^{-1}(N \cdot \mathbf{e}_0 \mathbf{e}_0^\top - \mathbf{I}) \mathbf{F}$ remains full-rank for $N \geq 2$ making the *error identical to low-rank approximation*, without any benefits from the additional computation:

$$\rho_{\text{D} \rightarrow \text{LoR}}^2(\mathbf{A}) = \frac{\|\mathbf{A} - (\text{diag}(\mathbf{A}) + \llbracket \bar{\mathbf{A}} \rrbracket_k)\|_{\text{F}}^2}{\|\mathbf{A}\|_{\text{F}}^2} = \frac{\|\bar{\mathbf{A}} - \llbracket \bar{\mathbf{A}} \rrbracket_k\|_{\text{F}}^2}{\|\mathbf{A}\|_{\text{F}}^2} = \frac{N - k}{N^2 + 3N} = \rho_{\text{LoR}}^2(\mathbf{A}).$$

Low-rank-then-diagonal. We reverse the order, starting with low-rank deflation followed by diagonal estimation of the residual, i.e. $\hat{\mathbf{A}} = \llbracket \mathbf{A} \rrbracket_k + \text{diag}(\mathbf{A} - \llbracket \mathbf{A} \rrbracket_k)$. The residual has the form $\mathbf{A} - \llbracket \mathbf{A} \rrbracket_k = \sum_{i=k}^{N-1} \mathbf{f}_i \mathbf{f}_i^*$ ($k \geq 1$), and we get the following recovery error (see Section A.2):

$$\rho_{\text{LoR} \rightarrow \text{D}}^2(\mathbf{A}) = \frac{\|\mathbf{A} - \llbracket \mathbf{A} \rrbracket_k + \text{diag}(\mathbf{A} - \llbracket \mathbf{A} \rrbracket_k)\|_{\text{F}}^2}{\|\mathbf{A}\|_{\text{F}}^2} = \frac{k/N - k^2/N^2}{N + 3}$$

While strictly better than ρ_{LoR}^2 (for $k < N$), the error does not decrease monotonically as k increases, making the optimal trade-off between low-rank deflation and diagonal estimation non-trivial.

These bounds (Fig. 1, right) underscore the inherent limitations of non-joint methods. Crucially, a perfect joint LoRD recovery, would achieve zero error for this example operator.

3.2 Empirical verification for sketched methods

We now empirically extend our findings for sketched variants of the strategies described in Section 3.1. The goal is to evaluate their practical performance when limited to a small number of MVP measurements, which we consider to be the primary bottleneck in this scenario. We thus prioritize measurement efficiency in our baseline to ensure a fair comparison. Specifically, we estimate diagonal components using XDIAG (Epperly et al. [2024], Alg. 5) and low-rank components via an SSVD (Tropp et al. [2017], Alg. 3). These also form the building blocks for the sequential strategies. D \rightarrow LoR (Alg. 7) first estimates the diagonal via XDIAG and then uses the SSVD on the residual. Since XDIAG performs an initial low-rank deflation, as part of its internal mechanism, we can reuse these measurements also for the SSVD, making this baseline more measurement efficient than a naive implementation. Conversely in LoR \rightarrow D (Alg. 6), we already perform a low-rank deflation via the SSVD, and can thus bypass the initial deflation step in the XDIAG method and directly apply the Girard-Hutchinson method, reminiscent of methods like DIAG++. This, again, optimizes the baseline in terms of measurement efficiency, providing a simple yet fair comparison.

Figure 1 contrasts theoretical error bounds (right panel) with the empirical performance of sketched algorithms (left: single-pass, center: oversampled recovery strategy) for the model operator $\mathbf{A} \in \mathbb{R}^{200 \times 200}$.² The empirical results reinforce the need for joint LoRD recovery uncovered in our theoretical analysis. As expected, all algorithms yield recovery errors equal or larger than the

²While the center and left panels show the empirical performance vs. the number of measurements p , the right panel shows the theoretical error bound vs. the rank k of an ideal recovery. However, since $p = \mathcal{O}(k)$, this serves as a useful estimate also vs. the number of measurements p .

respective theoretical lower bound. Individual approximation methods perform suboptimally, and the sequential methods offer only little improvement. $\text{LoR} \rightarrow \text{D}$ is only marginally better than a low-rank only approach, while $\text{D} \rightarrow \text{LoR}$ performs worse here. In stark contrast, a joint recovery approach (represented by SKETCHLORD, introduced in Section 4) achieves significantly lower error, often by many orders of magnitude, for the same number of measurements. This empirical evidence strongly underlines the necessity of algorithms explicitly designed for joint LoRD recovery when encountering operators with this composite structure.

4 Sketched low-rank plus diagonal approximations

This section details our core contribution: a scalable method for estimation of Low-Rank plus Diagonal (LoRD) operators. We first introduce a sketched mechanism and constraint that allow us to express joint low-rank and diagonal estimation as a convex optimization problem (Section 4.1). This formulation leads to our scalable strategy, called SKETCHLORD (Alg. 1), which we refine with several accelerations critical for practical efficiency (Section 4.2).

4.1 A convex optimization strategy

Consider a square³ linear operator $\mathbf{A} \in \mathbb{C}^{N \times N}$ that is only accessible via (costly) MVP measurements, $\mathbf{m} = \mathbf{A}\omega$, but admits a low-rank plus diagonal decomposition $\mathbf{A} =: \mathbf{L} + \mathbf{D}$, for $\text{rank}(\mathbf{L}) = k \ll N$ and $\mathbf{D} := \text{diag}(\mathbf{d})$. Since this decomposition is not necessarily unique (consider e.g. scalar matrices), we are interested in a rank-minimal solution:

$$(P_+) \quad \mathbf{L}_\natural, \mathbf{d}_\natural = \arg \min_{\mathbf{L}, \mathbf{d}} \text{rank}(\mathbf{L}) \quad \text{s.t.} \quad \mathbf{L} = \mathbf{A} + \text{diag}(\mathbf{d}) \quad (7)$$

This characterization is generally NP-hard [Natarajan, 1995] and the constraint involves unknown quantities \mathbf{A} and \mathbf{d} . To make it tractable, we will use a particular class of matrices $\Omega, \bar{\Omega} \in \mathbb{C}^{N \times p}$ satisfying $\Omega_{i,j} \bar{\Omega}_{i,j} = 1 \forall (i, j)$. We will also assume that it is possible to recover \mathbf{L} from $\mathbf{X} := \mathbf{L}\Omega$, which is true with high probability if Ω is random and we have enough measurements $p > k$ (Section 2). Then, the following sketching mechanism exposes an interesting structure:

$$\mathbf{M} := \mathbf{A}\Omega \circ \bar{\Omega} = \mathbf{L}\Omega \circ \bar{\Omega} + (\mathbf{D}\Omega) \circ \bar{\Omega} =: \mathbf{X} \circ \bar{\Omega} + \mathbf{d}\mathbf{1}^*. \quad (8)$$

Namely, that $\mathbf{d}\mathbf{1}^* = \mathbf{d}\mathbf{1}^* \frac{1}{p} (\mathbf{1}\mathbf{1}^*)$. This can be used to define a constraint that only depends on \mathbf{X} :

$$\mathbf{M} - \mathbf{X} \circ \bar{\Omega} = (\mathbf{M} - \mathbf{X} \circ \bar{\Omega}) \frac{1}{p} \mathbf{1}\mathbf{1}^* \Rightarrow \mathbf{M} \underbrace{(\mathbf{I} - \frac{1}{p} \mathbf{1}\mathbf{1}^*)}_{\tilde{\mathbf{M}}} = (\mathbf{X} \circ \bar{\Omega}) (\mathbf{I} - \frac{1}{p} \mathbf{1}\mathbf{1}^*) \quad (9)$$

This constraint defines a *feasible set* of candidate solutions \mathbf{X} , and it is easy to verify that \mathbf{L}_\natural is always contained in this set. This, combined with the fact that we assumed sufficient measurements for recovery, i.e. $\text{rank}(\mathbf{L}) = \text{rank}(\mathbf{L}\Omega)$, allows us to express our original problem in the following more tractable, re-parametrized form:

$$(P'_+ \equiv P_+) \quad \mathbf{X}_\natural = \arg \min_{\mathbf{X}} \text{rank}(\mathbf{X}) \quad \text{s.t.} \quad (\mathbf{X} \circ \bar{\Omega}) (\mathbf{I} - \frac{1}{p} \mathbf{1}\mathbf{1}^*) = \tilde{\mathbf{M}} \quad (10)$$

This is now an instance of the canonical low-rank problem reviewed in Section 2, which, as discussed, can be relaxed to the following equivalent Lagrangian for some unknown λ :

$$(P_\lambda \equiv P'_+) \quad \mathbf{X}_\natural = \arg \min_{\mathbf{X}} \underbrace{\frac{1}{2} \|\tilde{\mathbf{M}} - (\mathbf{X} \circ \bar{\Omega}) (\mathbf{I} - \frac{1}{p} \mathbf{1}\mathbf{1}^*)\|_F^2}_{\mathcal{L}_2} + \lambda \|\mathbf{X}\|_*, \quad (11)$$

And this can be optimized iteratively via $\mathbf{X} \leftarrow \mathcal{P}_\lambda(\mathbf{X} - \eta \nabla_{\mathbf{X}} \mathcal{L}_2)$ (Section 2), with the following gradient (see Section A.3 for a derivation):

$$\nabla_{\mathbf{X}} \mathcal{L}_2 = \left[\left((\mathbf{X} \circ \bar{\Omega}) - \tilde{\mathbf{M}} \right) (\mathbf{I} - \frac{1}{p} \mathbf{1}\mathbf{1}^*) \right] \circ \bar{\Omega}. \quad (12)$$

³The extension to non-square operators is supported in our code but omitted here for clarity.

Yielding the optimal $\mathbf{X}_{\natural} = \mathbf{L}_{\natural}\Omega$. Recall that we assumed a recovery of \mathbf{L}_{\natural} from \mathbf{X}_{\natural} is possible. One important caveat here is that this requires adjoint measurements from \mathbf{L}_{\natural} , the very operator we seek [Tropp et al., 2017, 3.5]. We resolve this by first isolating the diagonal component, and then performing deflated measurements as follows:

$$\mathbf{D}_{\natural} = 1/p \operatorname{diag}((\mathbf{M} - \mathbf{X}_{\natural} \circ \bar{\Omega})\mathbf{1}) \quad \text{and then} \quad \mathbf{\Upsilon}^* \mathbf{L}_{\natural} = (\mathbf{\Upsilon}^* \mathbf{A}) - (\mathbf{\Upsilon}^* \mathbf{D}_{\natural}) \quad (13)$$

With this, we can recover \mathbf{L}_{\natural} , finalizing the procedure. Putting everything together, we obtain SKETCHLORD, our full algorithm as presented in Alg. 1.

Algorithm 1: SKETCHLORD

```

Input:  $\mathbf{A} \in \mathbb{C}^{N \times N}$  // Linear operator
Input:  $\Omega, \mathbf{\Upsilon} \in \mathbb{C}^{N \times p}$  // Random matrices
Input:  $\eta, \lambda \in \mathbb{R}_{>0}$ 
// Forward random measurements
1  $\mathbf{M} \leftarrow \mathbf{A}\Omega \circ \bar{\Omega}$  //  $\mathbb{C}^{N \times p}$ 
// Constrained rank minimization
2  $\mathbf{X} \leftarrow \mathbf{M} \circ \Omega$ 
3 while not converged do
4    $\mathbf{X} \leftarrow \mathcal{P}_{\lambda}(\mathbf{X} - \eta \nabla_{\mathbf{X}} \mathcal{L}_2)$ 
5 end
// Diagonal recovery and adjoint measurements
6  $\mathbf{D} \leftarrow 1/p \operatorname{diag}((\mathbf{M} - \mathbf{X})\mathbf{1})$  //  $\mathbb{C}^N$ 
7  $\mathbf{W}^* \leftarrow (\mathbf{\Upsilon}^* \mathbf{A}) - (\mathbf{\Upsilon}^* \mathbf{D})$  //  $\mathbb{C}^{p \times N}$ 
// Recovery
8  $(\mathbf{U}, \Sigma, \mathbf{V}^*) \leftarrow \text{COMPACT}(\mathbf{M}, \Omega, \mathbf{W})$ 
9 return  $(\mathbf{U}, \Sigma, \mathbf{V}^*), \mathbf{d}$  //  $\mathbf{U}\Sigma\mathbf{V}^* + \operatorname{diag}(\mathbf{d}) \approx \mathbf{A}$ 

```

Algorithm 2: COMPACT

```

Input:  $\mathbf{M}, \Omega, \mathbf{W} \in \mathbb{C}^{N \times p}$ 
1  $(\mathbf{P}, \mathbf{S}) \leftarrow \operatorname{qr}(\mathbf{M})$  //  $\mathbb{C}^{N \times p}$ 
2  $(\mathbf{Q}, \mathbf{R}) \leftarrow \operatorname{qr}(\mathbf{W})$  //  $\mathbb{C}^{N \times p}$ 
3  $\mathbf{B} \leftarrow \mathbf{Q}^* \Omega$  //  $\mathbb{C}^{p \times p}$ 
4  $\mathbf{\Psi} \leftarrow \mathbf{S}\mathbf{B}^{\dagger}$  //  $\mathbb{C}^{p \times p}$ 
5  $\mathbf{Z}, \Sigma^2 \leftarrow \operatorname{eigh}(\mathbf{\Psi}^* \mathbf{\Psi})$  //  $\mathbb{C}^{p \times p}$ 
6  $\mathbf{V} \leftarrow \mathbf{Q}\mathbf{Z}$  //  $\mathbb{C}^{p \times p}$ 
7  $\mathbf{U} \leftarrow \mathbf{P}(\mathbf{B}\mathbf{S}^{\dagger})^* \mathbf{Z}\Sigma$  //  $\mathbb{C}^{N \times p}$ 
8 return  $(\mathbf{U}, \Sigma, \mathbf{V}^*)$ 

```

4.2 The SKETCHLORD algorithm

Overall, SKETCHLORD can be seen as an extension of ssvd (Alg. 3) featuring additional rank-minimization and diagonal deflation steps between measurements and recovery. But in reality, we incorporate a few modifications that make it practical, highlighted in Fig. 2 and discussed below:

Gradient momentum. In [Nesterov, 1983] it was shown that adding gradient momentum accelerates convergence substantially. We observed that this is also the case in our setting.

Optimal initialization. From Section A.3, we see that the \mathcal{L}_2 objective is minimized at the zero-gradient value, i.e. $\mathbf{X}_{opt} = \mathbf{M} \circ \Omega$. Initializing \mathbf{X} like this already positions it in the feasible set, resulting in faster convergence and stabler behavior, particularly with momentum.

Early termination. Optimal initialization leads to stable behavior of $\|\mathbf{X}\|_*$, monotonically decreasing and then stabilizing. This allows for a straightforward and fully automated way of identifying when to stop the optimization: We run an exponential moving average gathering the change in L_1 loss from one iteration to the next one, and when it is close enough to zero, the optimizer terminates. This makes the algorithm adaptive: if more deflation is needed, it will run for longer.

Compact recovery. The SINGLEPASS recovery method from Tropp et al. [2017] (Alg. 4) is scalable since it avoids performing more expensive measurements of \mathbf{A} . However, it still requires to perform numerical routines with $N \times p$ (i.e. *thin*) operators, which can be time-consuming for large N [e.g. Fernandez et al., 2025]. Here, we propose a COMPACT recovery method (Alg. 2) that relies for the most part on $p \times p$ (i.e. *compact*) operations. Following Halko et al. [2011], we first QR-decompose our random measurements as $\mathbf{X} =: \mathbf{P}\mathbf{S}$ and $\mathbf{W} =: \mathbf{Q}\mathbf{R}$, such that $\mathbf{L} \approx \mathbf{P}\mathbf{P}^* \mathbf{L} \mathbf{Q} \mathbf{Q}^*$. But, instead of discarding \mathbf{S} , we incorporate it in the derivations as follows:

$$\mathbf{P}\mathbf{S} = \underbrace{\mathbf{U}\Sigma\mathbf{V}^*}_{\mathbf{L}} \Omega \approx \mathbf{U}\Sigma \underbrace{\mathbf{V}^*\mathbf{Q}}_{\mathbf{Z}^*(\text{unitary})} \underbrace{\mathbf{Q}^*\Omega}_{\mathbf{B}} \Rightarrow \begin{cases} (\mathbf{S}\mathbf{B}^{\dagger})^* (\mathbf{S}\mathbf{B}^{\dagger}) \approx \mathbf{Z}\Sigma^2 \mathbf{Z}^* \Rightarrow \mathbf{V} \approx \mathbf{Q}\mathbf{Z} \\ \mathbf{P} \approx \mathbf{U}\Sigma \mathbf{Z} \mathbf{B} \mathbf{S}^{\dagger} \Rightarrow \mathbf{U} \approx \mathbf{P}(\Sigma \mathbf{Z} \mathbf{B} \mathbf{S}^{\dagger})^* \end{cases} \quad (14)$$

As a result, we see that both pseudo-inverses are indeed *compact*. This recovery also features a $p \times p$ Hermitian eigendecomposition, instead of an $N \times p$ SVD. In exchange, this method requires two $N \times p$ QR decompositions instead of one. In terms of stability we note that, since \mathbf{P} and \mathbf{Q} are

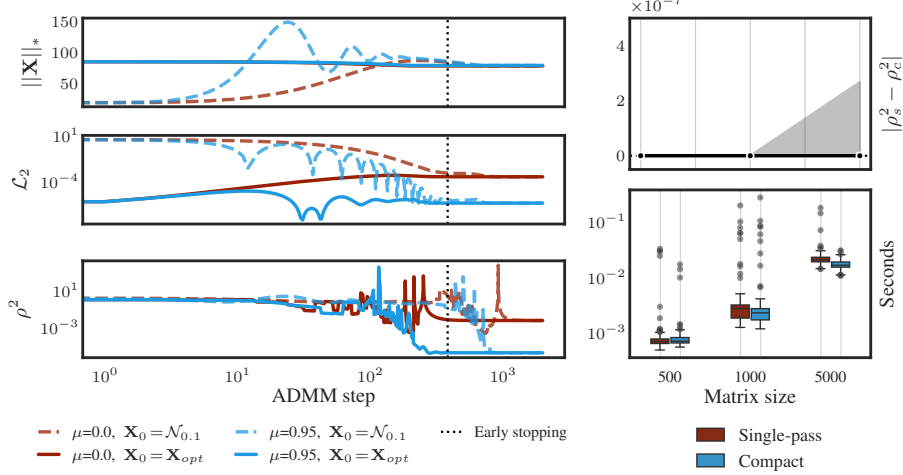


Figure 2: **SKETCHLORD accelerations:** (Left) Evolution of the P_λ losses from Eq. (11) as a function of optimization step, together with the energy error metric ρ defined in Eq. (5). We see that gradient momentum (blue) provides faster and better convergence, and we also see that an optimal initialization (solid lines) helps with performance and stability, particularly in combination with momentum. We also see how our simple early stopping strategy (evaluated here on the run with momentum and optimal initialization) correctly and efficiently predicts convergence of ρ . (Bottom right) Already for small scales, our proposed compact recovery provides a visible speedup, which is projected to improve as problems grow in size. (Top right) The ρ difference between our proposed COMPACT recovery (Alg. 2) and SINGLEPASS (Alg. 4) is negligible, supporting the benefit of our approach.

orthonormal, our pseudoinverses retain the same good condition as the ones from Tropp et al. [2017]. We empirically verify this, by comparing the recovery error ρ^2 and runtime for both single-pass and compact methods. We observe a speedup, even at small scales, without any performance degradation (Figure 2). This modest speedup is expected to grow at larger scales (see Golub and Van Loan [2013, 5.5] for asymptotics). Importantly, this proposed compact recovery is not SKETCHLORD-specific and can directly replace single-pass steps in other sketched algorithms (see Section 5).

4.3 Stability and Versatility

With the accelerations introduced in last section SKETCHLORD has 5 hyperparameters: step size and momentum for the gradient step (η, μ), threshold for the shrinkage step (λ), μ and a decay/tolerance for the early termination (i.e. the exponential moving average). Here, we focus on (η, μ, λ) , studying their relation and showing that the behavior of SKETCHLORD is stable across many configurations.

Table 1: **Convergence results for different hyperparameters:** See Section 4.3 for discussion.

η	λ	μ	Iterations	$\rho_{tot}^2 (\downarrow)$	$\rho_{diag}^2 (\downarrow)$	Convergence
1	0.05	0.95	492.4(52.7)	$(4.04 \pm 4.75) \times 10^{-3}$	$(5.34 \pm 2.05) \times 10^{-3}$	***
0.5	0.05	0.95	504.9(67.1)	$(3.20 \pm 4.63) \times 10^{-2}$	$(2.88 \pm 2.35) \times 10^{-2}$	**
0.25	0.05	0.95	557.7(22.0)	$(7.42 \pm 15.00) \times 10^{-2}$	$(8.96 \pm 10.30) \times 10^{-2}$	**
0.125	0.05	0.95	553.9(26.0)	$(1.10 \pm 1.34) \times 10^{-1}$	$(2.09 \pm 6.41) \times 10^{-1}$	*
1	0.2	0.95	582.7(36.2)	$(5.30 \pm 1.57) \times 10^{-1}$	$(3.47 \pm 8.96) \times 10^{-1}$	*
1	0.1	0.95	564.0(33.6)	$(1.22 \pm 2.74) \times 10^{-1}$	$(9.45 \pm 1.99) \times 10^{-2}$	**
1	0.025	0.95	536.0(0.0)	$(5.03 \pm 1.19) \times 10^{-3}$	$(4.07 \pm 8.04) \times 10^{-3}$	***
1	0.0125	0.95	443.4(62.0)	$(6.32 \pm 1.48) \times 10^{-4}$	$(6.07 \pm 0.86) \times 10^{-4}$	****
0.5	0.025	0.95	522.4(26.1)	$(4.02 \pm 4.90) \times 10^{-3}$	$(5.19 \pm 2.09) \times 10^{-3}$	***
0.25	0.0125	0.95	462.0(77.5)	$(4.22 \pm 4.76) \times 10^{-3}$	$(5.22 \pm 2.07) \times 10^{-3}$	***
0.5	0.025	0.99	2240.1(294.0)	$(1.00 \pm 3.14) \times 10^{-2}$	$(6.29 \pm 1.92) \times 10^{-3}$	**
0.25	0.0125	0.99	2201.9(328.9)	$(9.50 \pm 2.98) \times 10^{-3}$	$(5.83 \pm 1.78) \times 10^{-3}$	**
0.5	0.025	0.5	1092.7(3.6)	4.73 ± 9.73	2.60 ± 4.70	\emptyset
0.25	0.0125	0.5	2109.7(6.3)	4.70 ± 9.66	2.59 ± 4.66	\emptyset

For each hyperparameter configuration, we sample 10 $\exp(0.5)$ matrices with $N = 500$ (see [Section 5](#) and [Fig. 4](#)), and gathered recovery errors and runtimes. [Table 1](#) presents the main results, grouped in 5 sub-experiments: (a) Starting from a default, untuned parametrization, we explore values for η , observing that performance decreases with η . Note, due to the quadratic nature of the gradient-based objective, $\eta < 2$, to prevent divergence. (b) Then, we explore different values for λ , observing that performance is inversely proportional. (c) We then scale η & λ simultaneously, observing that performance remains virtually equal. Finally, we repeat the experiments from group (c) but with (d) larger and (e) smaller momentum. We observe that target performance is still invariant to λ/η , but extreme momentum values can drastically hinder performance. Our main conclusion is that the algorithm works fairly well for a broad range of hyperparameters as long as λ/η is large enough.

As we will see in the next section, this stability is paired with competitive performance on a broad class of matrices and great diagonal recovery ([Section A.5](#)). The downside of extra computations related to the ADMM optimization is easily offset by the fact that measurements are now bounded by $\text{rank}(L)$, not $\text{rank } A$. Furthermore, the early termination ties the amount of computation to deflation.

5 Synthetic experiments

To empirically validate our theoretical analysis ([Section 3](#)) and assess the practical performance of **SKETCHLORD**, we now conduct recovery experiments on an extensive suite of synthetic matrices. These experiments are designed to evaluate Low-Rank plus Diagonal (LoRD) recovery, from approximate LoRD but also purely low-rank matrices, and compare **SKETCHLORD** against established sketched baselines (see [Section 3.2](#)). Full details of the experimental setup, including matrix generation and hyperparameter settings, are provided in [Section A.4](#).

Experimental setup. We synthetically generate approximately LoRD matrices of the form $\mathbf{L} + \xi \mathbf{D}$, where \mathbf{L} is approximately low-rank and \mathbf{D} is a diagonal matrix. Following [Tropp et al. \[2019, 7.3.1\]](#), we construct \mathbf{L} using nine different matrix types, featuring three spectral decays (`exp`, `poly`, and `noise`) each with three different noise levels (denoted in parenthesis, e.g. $\exp(0.5)$). See [Fig. 4](#) for an illustration of these decays and the resulting matrices, and [Tropp et al. \[2019, 7.3.1\]](#) for details. The diagonal component \mathbf{D} is sampled from a Gaussian distribution, and its relative prominence is controlled by a factor ξ , which scales the diagonal's norm relative to the norm of \mathbf{L} . We test $\xi \in \{0, 0.1, 1, 10\}$, representing purely low-rank, weak diagonal, balanced, and strong diagonal dominance, respectively. For all cases, we evaluate three configurations, pairing matrix sizes $N \in \{500, 1000, 5000\}$ with corresponding approximate ranks $k \in \{10, 20, 100\}$ and the same measurement counts $p \in \{180, 360, 900\}$ for all methods, respectively. Lastly, we check all methods with three different recovery strategies (single-pass, oversampled, and compact) and 30 matrix samples per setting, resulting in more than 9000 evaluated matrices. All experiments are real-valued, and Rademacher random matrices are used for sketching, consistent with common practice. Our baselines include **XDIAG** for purely diagonal recovery, **SSVD** for purely low-rank approximations, and **D \rightarrow LoR** (Diagonal-then-Low-Rank) as well as **LoR \rightarrow D** (Low-Rank-then-Diagonal), with the implementation optimizations described in [Section 3.2](#). The approximation performance is primarily measured by the overall residual energy $\rho^2(\mathbf{A})$, i.e. the relative approximation error in Frobenius norm ([Eq. \(5\)](#)). We also capture the residual energy of only the diagonal part, to measure the algorithms' ability to accurately estimate diagonals.

Main results. Our synthetic experiments, summarized in [Fig. 3](#), with additional detailed plots in [Section A.5](#), reveal sever key insights into **SKETCHLORD**'s performance. **(I) Importance of joint recovery.** As the relative strength of the diagonal component (ξ) increases, **SKETCHLORD** increasingly shows stronger recovery performance, and the benefits of a joint recovery become more apparent. For matrices with a strong diagonal component, e.g. $\xi = 10$, **SKETCHLORD** consistently outperforms the baseline methods, often achieving recovery errors that are many order of magnitude lower. In those cases, neither a purely diagonal approximation (i.e. **XDIAG**) nor sequential approaches are sufficient to capture the composite structure. This highlights the critical operational regime where **SKETCHLORD** should be the preferred method. **(II) Efficiency of compact recovery.** Furthermore, the compact recovery strategy we introduced in [Section 4.2](#) yields nearly identical results that the standard single-pass recovery, while offering improved computational efficiency. **(III) Robustness in purely low-rank scenarios.** For purely low-rank matrices ($\xi = 0$), see [Figure 11](#), **SSVD** is the theoretically favored baseline and also empirically tends to yield the best results among the compared methods. However in many purely low-rank matrices, **SKETCHLORD** maintains

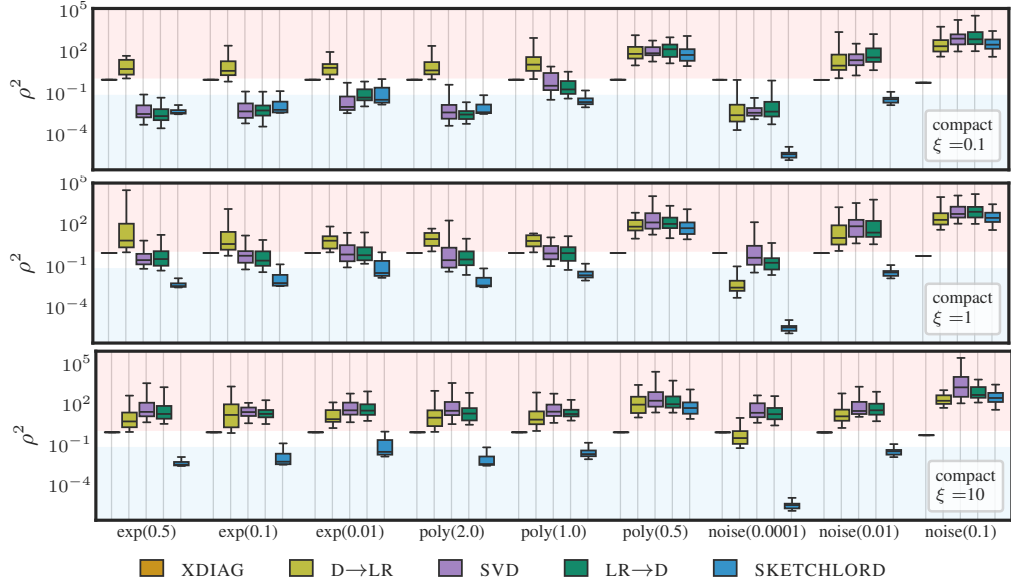


Figure 3: **SKETCHLORD provides high-fidelity approximations for LoRD matrices.** Recovery results for various random Low-Rank plus Diagonal (LoRD) matrices of size $N = 5000$. All matrices have an approximate rank $k = 100$ with rank noise of different intensities (see x-axis and Section A.4 for more explanation). The relative strength of the diagonal D is given by ξ and increases from the top to the bottom subplot. Provided are boxplots, across 30 samples each, of the recovery error for our studied algorithms, all from 900 measurements and COMPACT recovery (Alg. 2). Areas of $\rho^2 \geq 100\%$ relative error are shaded in red, and $\rho^2 \leq 10\%$ in blue.

commendable performance, sometimes even outperforming SSVD (e.g. `noise(0.0001)`) in terms of approximation quality. This resilience suggests SKETCHLORD’s versatility as drop-in alternative, even in cases where the presence or strength of a diagonal component in an operator is unknown.

In essence, SKETCHLORD successfully addresses scenarios where conventional sketched methods falter. For LoRD matrices, particularly those with strong diagonal parts, it offers substantially more accurate approximations, thereby expanding the scope of high-fidelity structured matrix recovery.

6 Conclusion

This paper addressed the suboptimal recovery of Low-Rank plus Diagonal (LoRD) operators by conventional sketched methods. We introduced SKETCHLORD, a sketched algorithm based on convex optimization and ADMM, for joint LoRD estimation. Experiments on synthetic data demonstrate SKETCHLORD’s ability to achieve high-fidelity approximations of composite LoRD structures.

Despite its strong performance, SKETCHLORD has limitations, some inherited from the nature of sketched methods, e.g. that the optimal noise structure for LoRD recovery is currently unknown. However, the most significant current drawback is the computational runtime, primarily due to the ADMM optimizer requiring a Singular Value Decomposition (SVD) in each iteration. We see several avenues to mitigate this. Future work could explore additional ADMM accelerations, such as incorporating quasi-Newton methods like L-BFGS [Liu and Nocedal, 1989] for the gradient step or FISTA [Beck and Teboulle, 2009] for the overall iteration. Additionally, optimizing directly on the singular space of the operator could allow pruning singular values as they approach zero during optimization, potentially reducing computational load and memory as optimization progresses. Beyond efficiency, the core framework of SKETCHLORD might be extendable: By vertically shifting the measurement operator $\bar{\Omega}$, we could target off-diagonal bands, potentially generalizing our method to the broader class of low-rank plus banded linear operators.

Ultimately, SKETCHLORD enriches the available toolkit of structured approximation techniques. While other methods may prioritize speed, SKETCHLORD distinguishes itself by delivering superior

approximation quality within a manageable memory footprint. It therefore offers a compelling option for scenarios where high fidelity is paramount, and the investment in runtime is justified by the significant gains in accuracy.

References

A. Beck and M. Teboulle. A fast iterative shrinkage-thresholding algorithm for linear inverse problems. *SIAM Journal on Imaging Sciences*, 2009.

C. Boutsidis, D. P. Woodruff, and P. Zhong. Optimal Principal Component Analysis in Distributed and Streaming Models. In *Proceedings of the Forty-Eighth Annual ACM Symposium on Theory of Computing*, 2016.

S. P. Boyd, N. Parikh, E. Chu, B. Peleato, and J. Eckstein. Distributed optimization and statistical learning via the alternating direction method of multipliers. *Foundations and Trends in Machine Learning*, 2011.

J.-F. Cai, E. J. Candès, and Z. Shen. A singular value thresholding algorithm for matrix completion. *SIAM Journal on Optimization*, 2010.

E. J. Candès and T. Tao. The power of convex relaxation: near-optimal matrix completion. *IEEE Transactions on Information Theory*, 2010.

E. J. Candès, X. Li, Y. Ma, and J. Wright. Robust principal component analysis? *Journal of the ACM*, 2011.

R. Couillet and M. Debbah. Signal processing in large systems: A new paradigm. *IEEE Signal Processing Magazine*, 2013.

M. Dereziński and M. W. Mahoney. Recent and upcoming developments in randomized numerical linear algebra for machine learning. In *ACM SIGKDD Conference on Knowledge Discovery and Data Mining*, 2024.

E. N. Epperly, J. A. Tropp, and R. J. Webber. Xtrace: Making the most of every sample in stochastic trace estimation. *SIAM Journal on Matrix Analysis and Applications*, 2024.

A. Fernandez, F. Schneider, M. Mahsereci, and P. Hennig. Connecting parameter magnitudes and hessian eigenspaces at scale using sketched methods. *Transactions on Machine Learning Research*, 2025. URL <https://openreview.net/forum?id=yGGo0VpBVP>.

B. Ghorbani, S. Krishnan, and Y. Xiao. An Investigation into Neural Net Optimization via Hessian Eigenvalue Density. In *International Conference on Machine Learning (ICML)*, 2019.

G. H. Golub and C. F. Van Loan. *Matrix Computations*. The Johns Hopkins University Press, 2013.

N. Halko, P. G. Martinsson, and J. A. Tropp. Finding Structure with Randomness: Probabilistic Algorithms for Constructing Approximate Matrix Decompositions. *SIAM Review*, 2011.

Y. Li, H. Nguyen, and D. Woodruff. Turnstile streaming algorithms might as well be linear sketches. *Proceedings of the Annual ACM Symposium on Theory of Computing*, 2014.

D. C. Liu and J. Nocedal. On the limited memory bfgs method for large scale optimization. *Math. Program.*, 45(1–3):503–528, Aug. 1989. ISSN 0025-5610.

J. Martens and R. Grosse. Optimizing Neural Networks with Kronecker-Factored Approximate Curvature. In *International Conference on Machine Learning (ICML)*, 2015.

B. K. Natarajan. Sparse approximate solutions to linear systems. *SIAM Journal on Computing*, 1995.

Y. Nesterov. A method of solving a convex programming problem with convergence rate $o(1/k^2)$. 1983.

V. Papyan. The Full Spectrum of Deepnet Hessians at Scale: Dynamics with SGD Training and Sample Size. *arXiv: Learning*, 2018.

B. A. Pearlmutter. Fast Exact Multiplication by the Hessian. *Neural Computation*, 1994.

K. B. Petersen and M. S. Pedersen. The matrix cookbook, 2012.

L. Sagun, U. Evci, V. U. Guney, Y. Dauphin, and L. Bottou. Empirical Analysis of the Hessian of Over-Parametrized Neural Networks, 2018. ICLR Workshop.

R. Tomioka and T. Suzuki. Regularization strategies and empirical bayesian learning for mkl. *ArXiv*, abs/1011.3090, 2010. URL <https://api.semanticscholar.org/CorpusID:2449064>.

J. A. Tropp, A. Yurtsever, M. Udell, and V. Cevher. Practical sketching algorithms for low-rank matrix approximation. *SIAM Journal on Matrix Analysis and Applications*, 2017.

J. A. Tropp, A. Yurtsever, M. Udell, and V. Cevher. Streaming low-rank matrix approximation with an application to scientific simulation. *SIAM Journal on Scientific Computing*, 2019.

A Appendix

A.1 Additional algorithms

This section provides additional pseudocode and background for the sketched algorithms involved in our experiments, in addition to the novel ones already provided in Section 4.

The original version of the SSVD (for *Sketched SVD*) algorithm was introduced in Halko et al. [2011]. This version featured a recovery step that requires a *second round of measurements* from the linear operator \mathbf{A} , and for this reason is not considered here. Instead, we gather in Alg. 3 the version from Tropp et al. [2017], which features a SINGLEPASS recovery (alg. 4) that *does not require any extra measurements*. This is also the case for our proposed COMPACT recovery (Alg. 2).

An OVERSAMPLED recovery, gathered in Alg. 8, was introduced in Boutsidis et al. [2016]. This recovery requires *extra measurements, but they can be fully parallelized*. In exchange for the extra measurements, it was shown in Tropp et al. [2019]—and is confirmed by our experiments—that it leads to better approximations, particularly in scenarios like streaming settings or slowly decaying spectra. We note that *any of the three recovery algorithms can be used exchangeably for any of the sketched methods*, and we do so in our experiments (see results in Section A.5).

Lastly, we have the algorithms discussed in Section 3.2: XDIAG (introduced in Epperly et al. [2024] and gathered in Alg. 5), and our two *sequential* baselines: LoR→D (Alg. 6) and D→LoR (Alg. 7).

Algorithm 3: SSVD [Tropp et al., 2017]

```

Input:  $\mathbf{A} \in \mathbb{C}^{N \times N}$  // Linear operator
Input:  $\Omega, \Upsilon \in \mathbb{C}^{N \times p}$  // Random matrices
// Random measurements
1  $\mathbf{M} \leftarrow \mathbf{A}\Omega$  //  $\mathbb{C}^{N \times p}$ 
2  $\mathbf{W}^* \leftarrow \Upsilon^* \mathbf{A}$  //  $\mathbb{C}^{p \times N}$ 
// Recovery  $(\mathbf{U}, \mathbf{V} \in \mathbb{C}^{N \times p})$ 
3  $(\mathbf{U}, \Sigma, \mathbf{V}^*) \leftarrow \text{SINGLEPASS}(\mathbf{M}, \Omega, \mathbf{W})$ 
return  $(\mathbf{U}, \Sigma, \mathbf{V}^*)$  //  $\mathbf{U}\Sigma\mathbf{V}^* \approx \mathbf{A}$ 

```

Algorithm 4: SINGLEPASS [Tropp et al., 2017]

```

Input:  $\mathbf{M}, \Omega, \mathbf{W} \in \mathbb{C}^{N \times p}$ 
1  $(\mathbf{P}, \_) \leftarrow \text{qr}(\mathbf{W})$  //  $\mathbb{C}^{N \times p}$ 
2  $\mathbf{B} \leftarrow \mathbf{M}(\mathbf{P}^* \Omega)^\dagger$  //  $\mathbb{C}^{N \times p}$ 
3  $(\mathbf{U}, \Sigma, \mathbf{Z}^*) \leftarrow \text{svd}(\mathbf{B})$  //  $\mathbb{C}^{N \times p}, \mathbb{C}^{p \times p}, \mathbb{C}^{p \times p}$ 
4  $\mathbf{V} \leftarrow \mathbf{P}\mathbf{Z}$  //  $\mathbb{C}^{N \times p}$ 
5 return  $(\mathbf{U}, \Sigma, \mathbf{V}^*)$ 

```

Algorithm 5: XDIAG [Epperly et al., 2024, 2.1]

```

Input:  $\mathbf{A} \in \mathbb{C}^{N \times N}$  // Linear operator
Input:  $\Omega \in \mathbb{C}^{N \times p}$  // Rademacher matrix
// Random measurements and XDiag matrix
1  $\mathbf{M} \leftarrow \mathbf{A}\Omega$  //  $\mathbb{C}^{N \times p}$ 
2  $(\mathbf{Q}, \mathbf{R}) \leftarrow \text{qr}(\mathbf{M})$ 
3  $\mathbf{S} \leftarrow \text{norm}(\mathbf{R}^\dagger)$  // column normalization
4  $\Psi \leftarrow \mathbf{I} - 1/p \mathbf{S}\mathbf{S}^*$  //  $\mathbb{C}^{p \times p}$ 
// Top-space diagonal estimation
5  $\mathbf{X}^* \leftarrow \mathbf{S}\mathbf{Q}^* \mathbf{A}$ 
6  $\mathbf{d} \leftarrow (\mathbf{Q} \circ \mathbf{X}^*)\mathbf{1}$ 
// Bottom-space diagonal estimation
7 for  $i \in \{1, \dots, p\}$  do
8    $| \mathbf{d} \leftarrow \mathbf{d} + [1/p \omega_i \odot (\mathbf{m}_i - \mathbf{Q}\mathbf{X}^*\omega_i)]$ 
9 end
10 return  $(\mathbf{d}, \mathbf{Q})$  //  $\mathbf{d} \approx \text{diag}(\mathbf{A})$ 

```

Algorithm 6: LoR→D

```

Input:  $\mathbf{A} \in \mathbb{C}^{N \times N}$  // Linear operator
Input:  $\Omega, \Upsilon, \Gamma \in \mathbb{C}^{N \times p}$  // Rademacher matrices
1  $(\mathbf{U}, \Sigma, \mathbf{V}^*) \leftarrow \text{SSVD}(\mathbf{A}, \Omega, \Upsilon)$ 
2  $\mathbf{B} \leftarrow (\mathbf{A} - \mathbf{U}\Sigma\mathbf{V}^*)$  // Implicit, matrix-free
3  $\mathbf{d} \leftarrow 1/p(\Gamma \odot \mathbf{B}\Gamma)\mathbf{1}$ 
4 return  $(\mathbf{U}, \Sigma, \mathbf{V}^*), \mathbf{d}$  //  $\mathbf{U}\Sigma\mathbf{V}^* + \text{diag}(\mathbf{d}) \approx \mathbf{A}$ 

```

Algorithm 7: D→LoR

```

Input:  $\mathbf{A} \in \mathbb{C}^{N \times N}$  // Linear operator
Input:  $\Omega, \Upsilon, \Gamma \in \mathbb{C}^{N \times p}$  // Rademacher matrices
1  $(\mathbf{d}, \mathbf{Q}) \leftarrow \text{XDIAG}(\mathbf{A}, \Omega)$ 
// asdf
2  $\mathbf{M} \leftarrow \mathbf{A}\Omega - \text{diag}(\mathbf{d})\Omega$  // Recycled from XDiag
3  $\mathbf{W}^* \leftarrow \Upsilon^* \mathbf{A} - \Upsilon^* \text{diag}(\mathbf{d})$ 
4  $(\mathbf{U}, \Sigma, \mathbf{V}^*) \leftarrow \text{COMPACT}(\mathbf{M}, \Omega\mathbf{W})$ 
5 return  $(\mathbf{U}, \Sigma, \mathbf{V}^*), \mathbf{d}$  //  $\mathbf{U}\Sigma\mathbf{V}^* + \text{diag}(\mathbf{d}) \approx \mathbf{A}$ 

```

Algorithm 8: OVERSAMPLED [Boutsidis et al., 2016, Tropp et al., 2019]

```

Input:  $\mathbf{A} \in \mathbb{C}^{N \times N}$  // Linear operator
Input:  $\mathbf{P}, \mathbf{Q} \in \mathbb{C}^{N \times p}$  // Orthogonalized sketches
Input:  $\Omega', \Upsilon' \in \mathbb{C}^{N \times 2p}$  // Random matrices
// Perform core measurements and solve core matrix
1  $\mathbf{C} \leftarrow \Upsilon'^* \mathbf{A} \Omega'$  //  $\mathbb{C}^{2p \times 2p}$ 
2  $\mathbf{C} \leftarrow (\Upsilon'^* \mathbf{P})^\dagger \mathbf{C} (\mathbf{Q}^* \Omega')^\dagger$  //  $\mathbb{C}^{p \times p}$ 
3  $(\mathbf{U}', \Sigma, \mathbf{V}'^*) \leftarrow \text{svd}(\mathbf{C})$ 
4  $\mathbf{U} \leftarrow \mathbf{P}\mathbf{U}'$  //  $\mathbb{C}^{N \times p}$  orthonormal
5  $\mathbf{V} \leftarrow \mathbf{Q}\mathbf{V}'$  //  $\mathbb{C}^{N \times p}$  orthonormal
6 return  $(\mathbf{U}, \Sigma, \mathbf{V}^*)$ 

```

A.2 Mathematical details for Section 3.1

Here, we provide a more detailed derivation for the error of a **low-rank-then-diagonal** approximation. In this approximation, we start with low-rank deflation followed by diagonal estimation of the residual, i.e. $\hat{\mathbf{A}} = [\mathbf{A}]_k + \text{diag}(\mathbf{A} - [\mathbf{A}]_k)$. By definition, and based on the Fourier eigendecomposition from Section 3.1, the residual has the form $\mathbf{A} - [\mathbf{A}]_k = \sum_{i=k}^{N-1} \mathbf{f}_i \mathbf{f}_i^*$ ($k \geq 1$), with scalar diagonal in the form $\text{diag}(\mathbf{A} - [\mathbf{A}]_k) = \frac{N-k}{N} \mathbf{I}$. Also recall that $\|\mathbf{A}\|_F^2 = N(N+3)$ and that the Fourier vectors \mathbf{f}_i form a unitary basis. With this, we derive the following recovery error:

$$\begin{aligned} \rho_{\text{LoR} \rightarrow \text{D}}^2(\mathbf{A}) &= \frac{\|\mathbf{A} - [\mathbf{A}]_k - \text{diag}(\mathbf{A} - [\mathbf{A}]_k)\|_F^2}{\|\mathbf{A}\|_F^2} = \frac{\|(\sum_{i=k}^{N-1} \mathbf{f}_i \mathbf{f}_i^*) - \frac{N-k}{N} \mathbf{I}\|_F^2}{N(N+3)} \\ &= \frac{1}{N(N+3)} \left(\sum_{i=k}^{N-1} \sum_{j=k}^{N-1} (\mathbf{f}_i^* \mathbf{f}_j)^2 + \frac{(N-k)^2}{N} - 2 \frac{N-k}{N} \sum_{i=k}^{N-1} (\mathbf{f}_i^* \mathbf{f}_i) \right) \\ &= \frac{(N-k) - \frac{(N-k)^2}{N}}{N(N+3)} = \frac{k/N - k^2/N^2}{N+3} \end{aligned}$$

A.3 Extended discussion on optimization strategy

Recall the \mathcal{L}_2 component from Eq. (11), derived from the equality constraint in Eq. (9):

$$\mathcal{L}_2 = \frac{1}{2} \|(\mathbf{M} - \mathbf{X} \circ \bar{\Omega})(\mathbf{I} - \frac{1}{p} \mathbf{1} \mathbf{1}^*)\|_F^2 \quad (15)$$

This can be equivalently expressed in vectorized form via Kronecker products as follows [Petersen and Pedersen, 2012, 10.2.2]:

$$\mathcal{L}_2 = \frac{1}{2} \left\| \left(\underbrace{\mathbf{I} - \left(\frac{1}{p} \mathbf{1} \mathbf{1}^* \otimes \mathbf{I} \right)}_{\Phi} \right) \left(\underbrace{\text{vec}(\mathbf{M})}_{\mathbf{m}} - \underbrace{\text{diag}(\text{vec}(\bar{\Omega}))}_{\bar{\mathbf{J}}} \underbrace{\text{vec}(\mathbf{X})}_{\mathbf{x}} \right) \right\|_2^2 = \frac{1}{2} \|\Phi \mathbf{m} - \Phi \bar{\mathbf{J}} \mathbf{x}\|_2^2 \quad (16)$$

Minimizing this loss is a classic linear least squares problem that, not only is *convex* w.r.t. \mathbf{x} , but also admits a *closed-form* expression for the gradient [Petersen and Pedersen, 2012, 5.1] that is particularly simple due to symmetry and idempotence of Φ :

$$\nabla_{\mathbf{x}} \mathcal{L}_2 = \frac{1}{2} (2 \bar{\mathbf{J}}^* \underbrace{\Phi^* \Phi}_{=\Phi} \bar{\mathbf{J}} \mathbf{x} - 2 \bar{\mathbf{J}} \Phi^* \Phi \mathbf{m}) = \bar{\mathbf{J}} \Phi (\bar{\mathbf{J}} \mathbf{x} - \mathbf{m}) \quad (17)$$

Which can be in turn expressed in matrix form by inverting the vectorization step, yielding the gradient as presented in Eq. (12):

$$\nabla_{\mathbf{X}} \mathcal{L}_2 = \bar{\Omega} \circ \text{vec}^{-1}(\Phi(\bar{\mathbf{J}} \mathbf{x} - \mathbf{m})) = \bar{\Omega} \circ ((\mathbf{X} \circ \bar{\Omega}) - \mathbf{M})(\mathbf{I} - \frac{1}{p} \mathbf{1} \mathbf{1}^*) \quad (18)$$

This derivation also yields a closed-form optimal value for \mathbf{X} that guarantees a value of zero for \mathcal{L}_2 and its gradient. In Section 4.2, we show that initializing the ADMM solver with this \mathbf{X}_{opt} value results in faster convergence and stabler behavior, particularly with momentum:

$$\mathbf{X}_{opt} = \mathbf{M} \circ \bar{\Omega} \Rightarrow \mathbf{X}_{opt} \circ \bar{\Omega} = \mathbf{M} \Rightarrow \begin{cases} \mathcal{L}_2 = 0 \\ \nabla_{\mathbf{X}} \mathcal{L}_2 = 0 \end{cases} \quad (19)$$

To conclude this section, we provide the derivation of \mathbf{D}_{\natural} from Eq. (13). Recall that $\mathbf{D} = \text{diag}(\mathbf{d})$ and $\mathbf{d} \mathbf{1}^* = \mathbf{M} - \mathbf{X} \circ \bar{\Omega}$. Then,

$$\mathbf{d} = \frac{1}{p} \mathbf{d} \mathbf{1}^* \mathbf{1} = \frac{1}{p} (\mathbf{M} - \mathbf{X} \circ \bar{\Omega}) \mathbf{1} \quad (20)$$

A.4 Synthetic Experiment Details

Low-rank plus diagonal matrices: We follow Tropp et al. [2019, 7.3.1] to sample three classes of *approximately* low-rank random matrices \mathbf{L} : (a) The $\exp(t)$ matrices feature k -many unit singular

Algorithm 9: Overview of the synthetic experimental setup discussed in Sections A.4 and 5. Each recovery algorithm features different hyperparametrizations and random matrix samples, which can be found in Section A.1. The step of gathering recovery metrics and runtimes is omitted here.

```

1 for  $(N, k, p) \in \{(500, 5, 90), (1000, 10, 180), (5000, 50, 900)\}$  // Matrix size, rank, #measurements
2 do
3   for  $\xi \in \{0, 0.1, 1, 10\}$  // Diagonal strength
4     do
5       for  $\mathcal{M} \in \{ \exp(0.5), \exp(0.1), \exp(0.01), \text{poly}(2), \text{poly}(1), \text{poly}(0.5),$ 
6            $\text{noise}(0.0001), \text{noise}(0.01), \text{noise}(0.1) \}$  // Low-rank matrix distribution
7         do
8           repeat 30 times
9              $\mathbf{L} \sim \mathcal{M}(N, k)$  // Low-rank component  $\mathbb{C}^{N \times N}$  of approximate rank  $k$ 
10             $\mathbf{d} \sim \mathcal{N}(0, \mathbf{I})$  // Diagonal component  $\mathbb{C}^N$ 
11             $\mathbf{A} \leftarrow \mathbf{L} + \xi \cdot \frac{\|\mathbf{L}\|_2 \sqrt{N}}{\|\mathbf{d}\|_2} \text{diag}(\mathbf{d})$ 
12            for  $\mathcal{S} \in \{ \text{SSVD}, \text{XDIAG}, \text{SKETCHLORD } D \rightarrow \text{LoR}, \text{LoR} \rightarrow D \}$  do
13              for  $\mathcal{R} \in \{ \text{SINGLEPASS}, \text{COMPACT}, \text{OVERSAMPLED} \}$  do
14                 $\hat{\mathbf{A}} \leftarrow \mathcal{S}_{\mathcal{R}}(\mathbf{A}, p)$  // Sketched estimation of  $\mathbf{A}$ 
15              end
16            end
17          end
18        end
19      end
20    end
21  end
22
```

values, and then the following singular values decay exponentially, at a rate given by t (see Figure 4): as t increases, the effective rank gets closer to k . The left and right singular spaces are sampled randomly. Following Tropp et al. [2019], we use t values of 0.5 (fast decay), 0.1 (medium) and 0.01 (slow). (b) The $\text{poly}(t)$ matrices are generated analogously to $\exp(t)$, with the difference that, after the k singular values of 1, the following ones decay polynomially instead of exponentially. Following Tropp et al. [2019], we use t values of 2 (fast decay), 1 (medium) and 0.5 (slow). (c) The $\text{noise}(t)$ matrices are the sum of 2 matrices: a low-rank matrix that just has k -many unit diagonal entries (the rest is zeros), plus a noisy matrix with a noise intensity of t . Following Tropp et al. [2019], we use t values of 0.0001 (low noise), 0.01 (medium) and 0.1 (high).

In order to make the sampled matrices low-rank *plus diagonal* (i.e. $\mathbf{L} + \mathbf{D}$), and still retain some control about the prominence of \mathbf{D} , we introduce a *diagonal ratio* parameter $\xi \in \mathbb{R}_{\geq 0}$: If $\xi = 0$, no diagonal should be added. A large ξ (e.g. 10) should mean that \mathbf{D} is very prominent, and for $\xi = 1$ it should be balanced. This is realized by the following ratio between their norms:

$$\mathbf{A} = \mathbf{L} + \xi \cdot \sqrt{\frac{\|\mathbf{L}\|_2^2}{N\|\mathbf{D}\|_2^2}} \mathbf{D} \quad (21)$$

We can see that, for $\xi = 1$, the squared norm of the added diagonal, which has N entries, equals the average squared norm of a vector from \mathbf{L} , which also has N entries. See Figure 4 for an illustration of this process and how it affects the appearance of the combined matrix, as well as its singular value distribution.

Sketched mechanism: We note that, although our derivation of the sketch in Section 4.1 applies to any complex-valued matrix, our experiments are performed in \mathbb{R} . In this case, the natural choice for random $\Omega, \bar{\Omega} \in \mathbb{C}^{N \times p}$ satisfying $\Omega_{i,j} \bar{\Omega}_{i,j} = 1 \forall (i, j)$ is to use Rademacher noise, since this is satisfied in an efficient and numerically stable manner for $\Omega = \bar{\Omega}$. While it would be interesting to explore other sources of noise, like SSRFT [Tropp et al., 2019, 3.2], it has been noted that the particular source of noise does not typically make much difference in practice [Tropp et al., 2017, 3.9]. Furthermore, Rademacher is a popular and well-studied source of sketching noise, including [Tropp et al., 2019, Epperly et al., 2024], which helps establishing comparisons.

Design choices: An overview of the experimental setup can be found in Alg. 9. We sample square (but not symmetric) LoRD matrices of 3 different sizes N , up to $N = 5000$. In order to decide the underlying rank k and number of sketched measurements p , we found that $k = N/100$ and $p = 18k$ exposed the regime in which algorithms would sometimes fail, and sometimes succeed at recovering the matrices (see Section A.5). We chose p to be a multiple of 6 in order to ensure that all compared

algorithms perform the exact same number of measurements (since some measure in groups of 2, and others in groups of 3). As previously explained, we sample low-rank matrices from 9 different classes following [Tropp et al. \[2019, 7.3.1\]](#), and add diagonal components following 4 ratios ξ : 0 (no added diagonal), 0.1 (weak), 1 (balanced) and 10 (strong). For each scenario, we sample 30 different random matrices, and provide error bars gathered across this population. And for each sample, we ran all sketched algorithms with all 3 possible recovery mechanisms, gathering runtimes and performance metrics.

Implementation: Performing the full experiment for each sample took ~ 18 hours on a distributed CPU cluster (i.e. ~ 540 hours total).

A.5 Synthetic Experiment, Extra Results

This section contains additional results from our experiments with synthetic matrices, extending [Section 5](#) and [Section A.4](#):

Full recovery line plots (Figures 5 to 7): These plots display the ρ^2 error between original and recovery, for all matrix types, algorithms, recoveries and diagonal ratios ξ . See [Eqs. \(5\)](#) and [\(21\)](#) for the definitions of ρ^2 and ξ , respectively. Note how, when one method fails, all methods tend to also fail (likely due to insufficient measurements). Given sufficient measurements, SKETCHLORD provides almost always the best recovery.

Diagonal recovery line plots (Figures 8 to 10): Same as above, but the ρ^2 error is measured between the *diagonal* of the original and the *diagonal* of the recovery. Thus, it measures the effectiveness in recovering the diagonal of a linear operator, even for cases when the operator itself is not diagonal. Note how, given enough measurements, the joint recovery strategy followed by SKETCHLORD also yields superior results, even compared to ad-hoc methods like XDIAG.

Low-rank recovery boxplots (Figure 11): In [Figure 3](#), the recovery error for various matrix types is provided, for cases where the diagonal component is nonzero. Here, we provide similar results but with $\xi = 0$, i.e. for the cases where the additional diagonal component is zero and just the low-rank component is present. Here, SKETCHLORD is also competitive, although generally not better than SSVD.

Runtime boxplots (Figures 12 and 13): SKETCHLORD features an ADMM optimization step that can take a variable number of steps until termination, and thus have an impact in the overall runtime. These plots provide the gathered number of iterations and runtimes across all matrix types, sizes and diagonal ratios. Interestingly, we observe that the ADMM runtime does not seem to depend on ξ : this may be due to excessively conservative values for the early termination scheme. Furthermore, ADMM seems to run longer for matrices of the *noise* type, even when the matrix is simple and the final recovery is good. This may also indicate early termination issues for those cases.

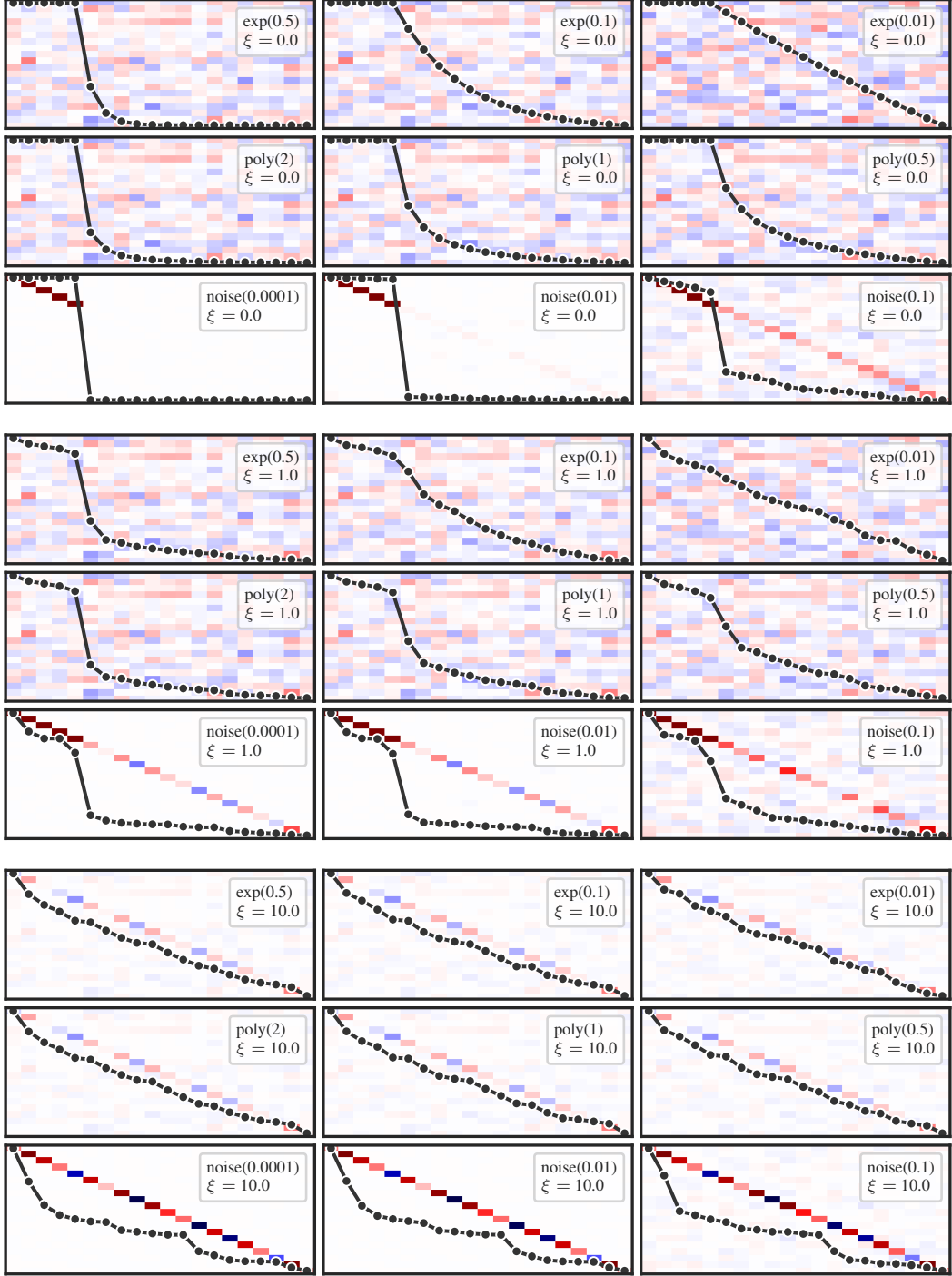


Figure 4: Different types of synthetic low-rank plus diagonal matrices, where ξ expresses the *relative importance* of the diagonal component. On top of each matrix, the corresponding distribution of singular values is provided, adjusted to fit the frame. See Section A.4 for more details.

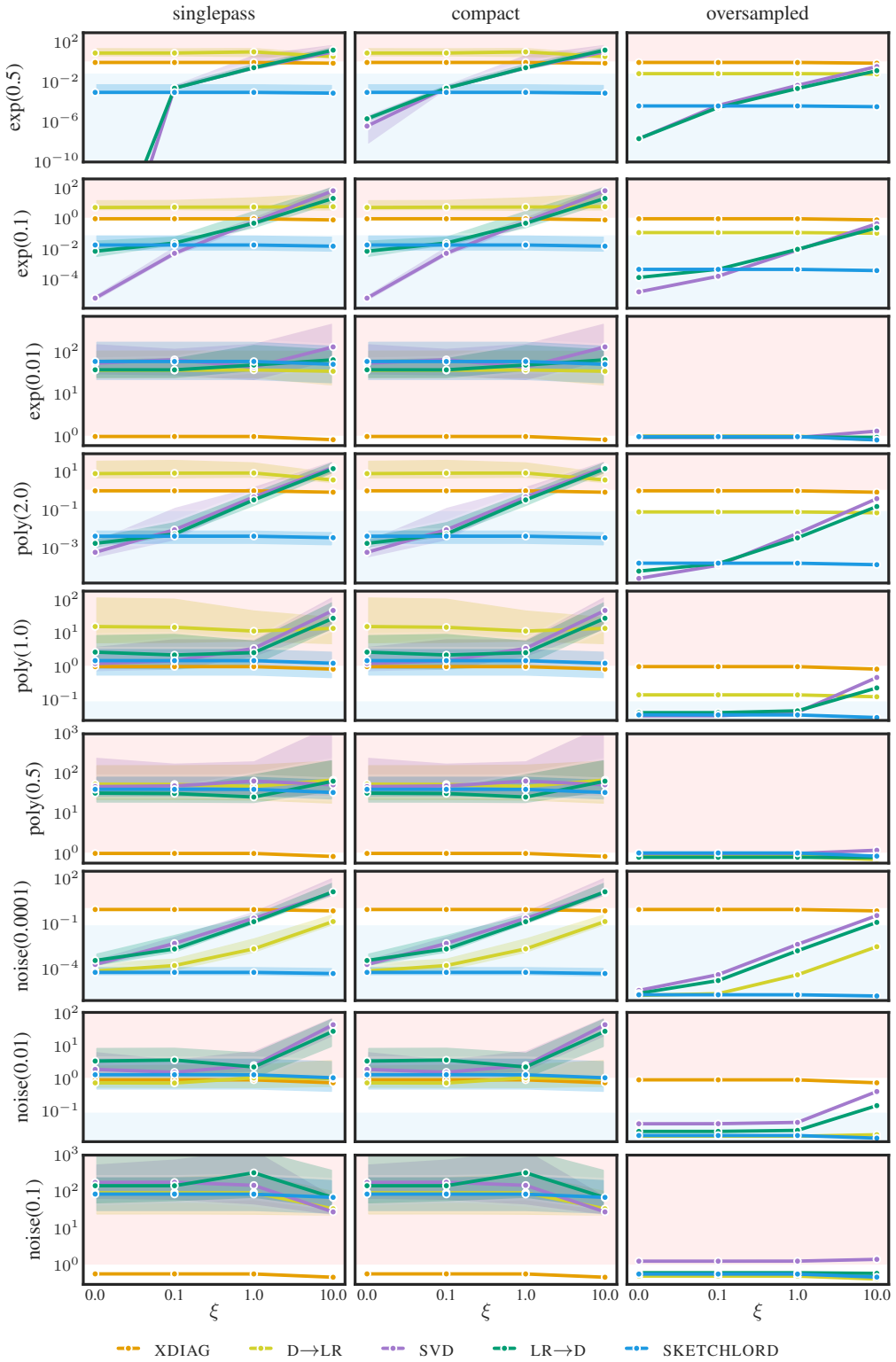


Figure 5: Residual energy (ρ^2) for the **full recovery** of 500×500 **matrices**, gathered following the protocol described in [Section A.4](#). Areas of 100% error and above are shaded in red. Areas of 10% error and below are shaded in blue. See [Sections A.4](#) and [A.5](#) for further details and discussion.

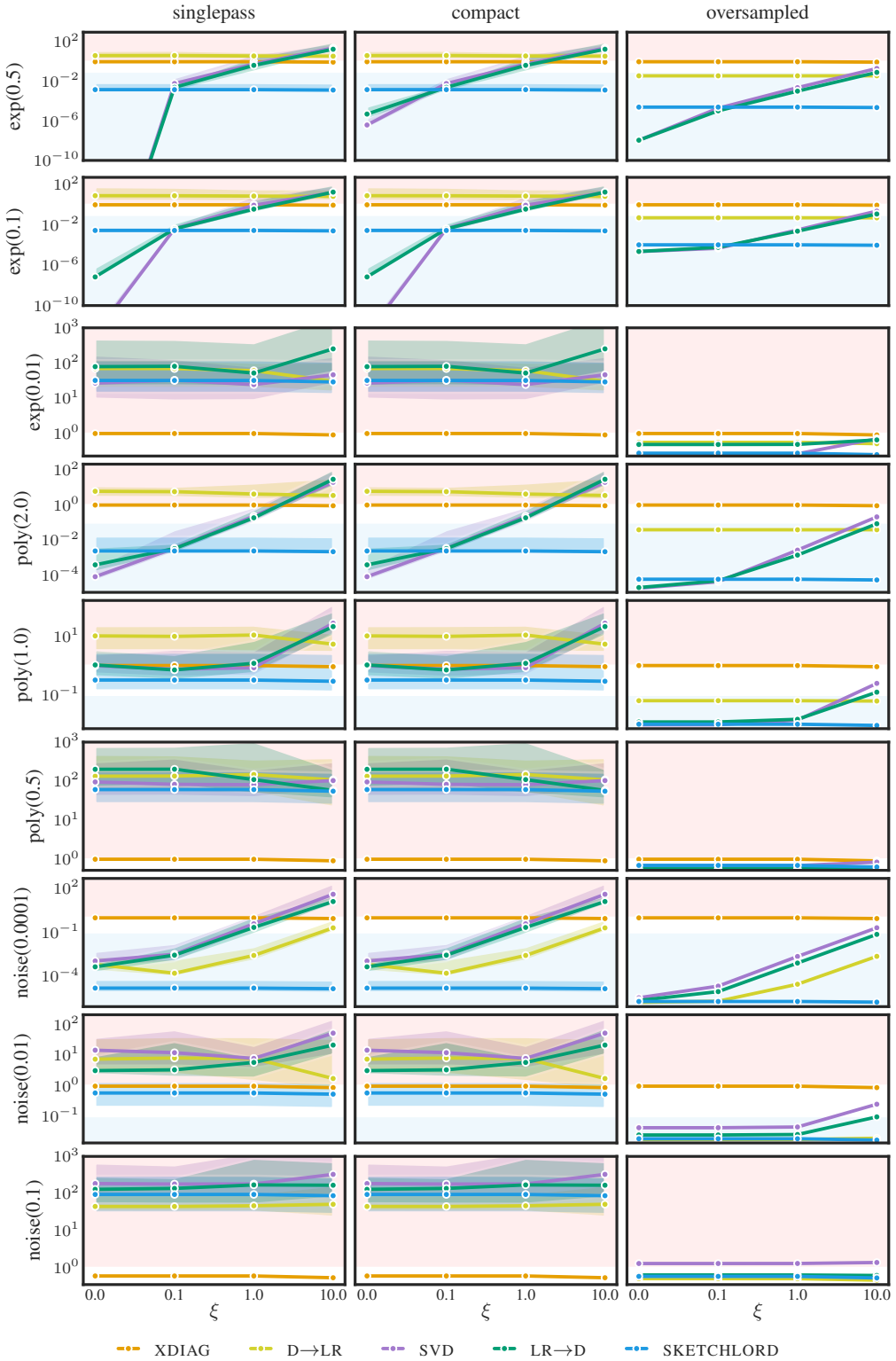


Figure 6: Residual energy (ρ^2) for the **full recovery** of 1000×1000 matrices, gathered following the protocol described in Section A.4. Areas of 100% error and above are shaded in red. Areas of 10% error and below are shaded in blue. See Sections A.4 and A.5 for further details and discussion.

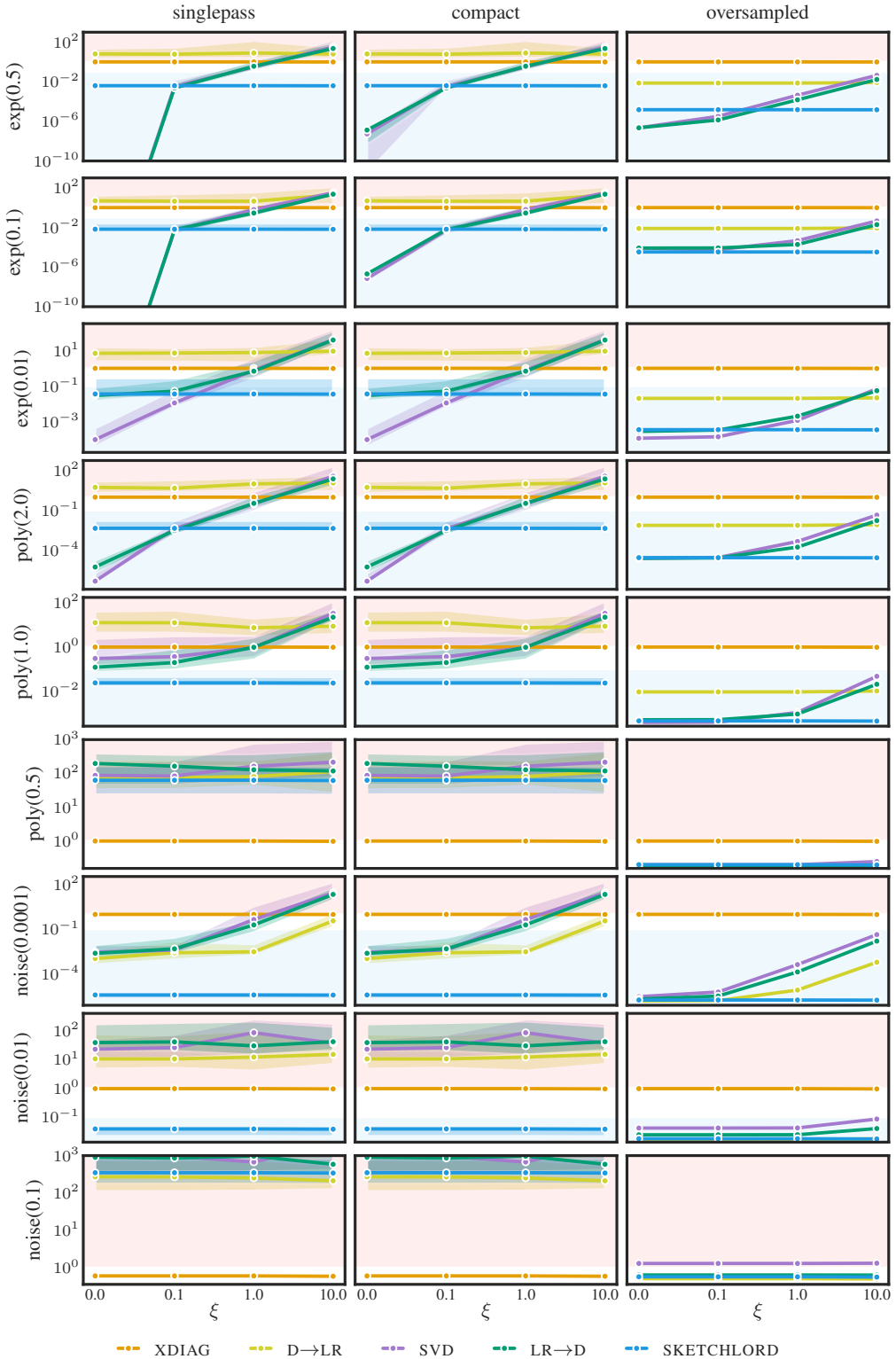


Figure 7: Residual energy (ρ^2) for the **full recovery** of 5000×5000 matrices, gathered following the protocol described in Section A.4. Areas of 100% error and above are shaded in red. Areas of 10% error and below are shaded in blue. See Sections A.4 and A.5 for further details and discussion.

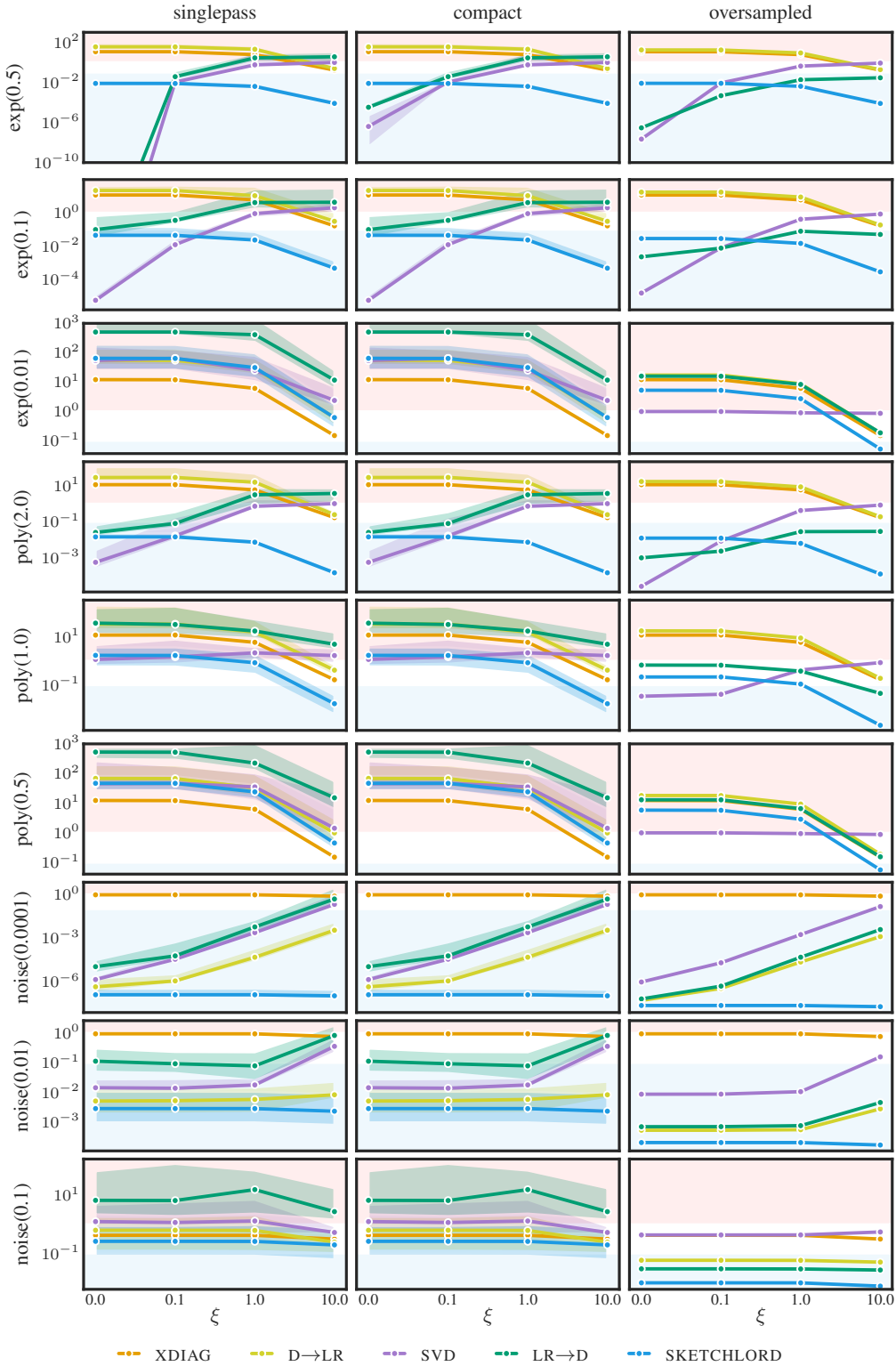


Figure 8: Residual energy (ρ^2) for the **diagonal recovery of 500×500 matrices**, gathered following the protocol described in Section A.4. Areas of 100% error and above are shaded in red. Areas of 10% error and below are shaded in blue. See Sections A.4 and A.5 for further details and discussion.

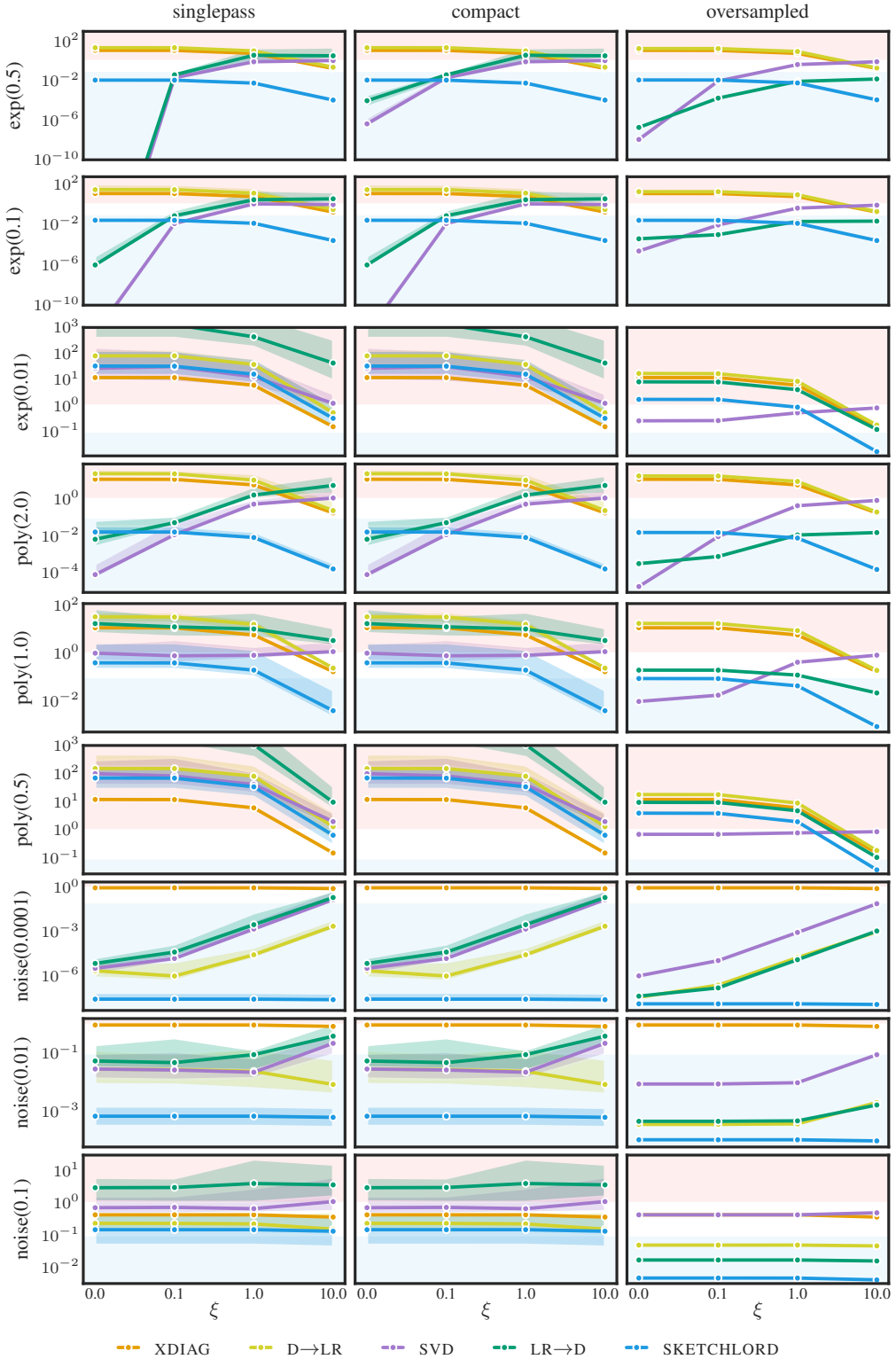


Figure 9: Residual energy (ρ^2) for the **diagonal recovery of** 1000×1000 **matrices**, gathered following the protocol described in Section A.4. Areas of 100% error and above are shaded in red. Areas of 10% error and below are shaded in blue. See Sections A.4 and A.5 for further details and discussion.

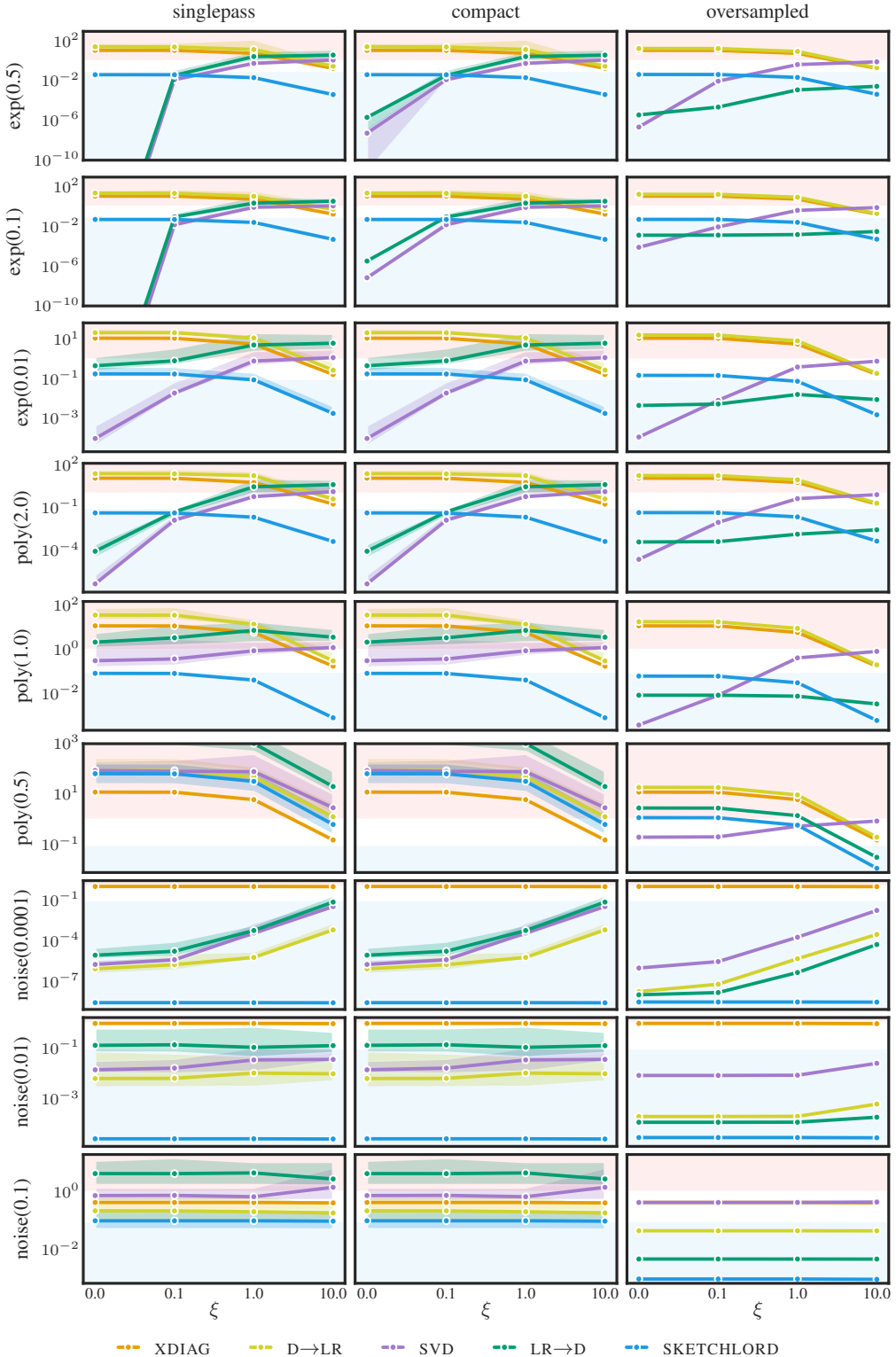


Figure 10: Residual energy (ρ^2) for the **diagonal recovery** of 5000×5000 matrices, gathered following the protocol described in Section A.4. Areas of 100% error and above are shaded in red. Areas of 10% error and below are shaded in blue. See Sections A.4 and A.5 for further details and discussion.

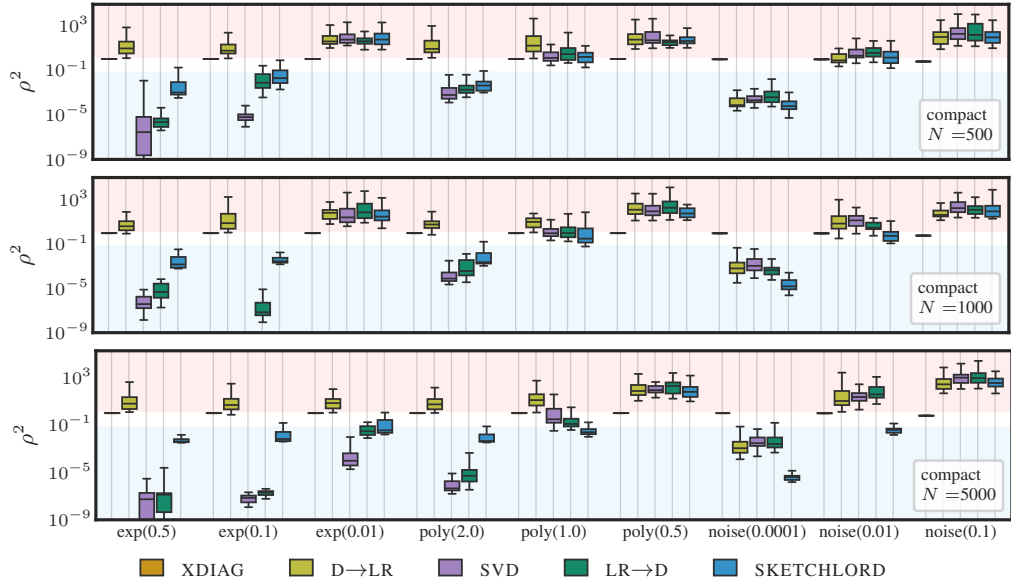


Figure 11: **SKETCHLORD is competitive for low-rank matrices, although generally not better than SSVD:** Recovery error for various matrix types and sizes at $\xi = 0$ (i.e. only the low-rank component is present). See Sections A.4 and A.5 for further details and discussion.

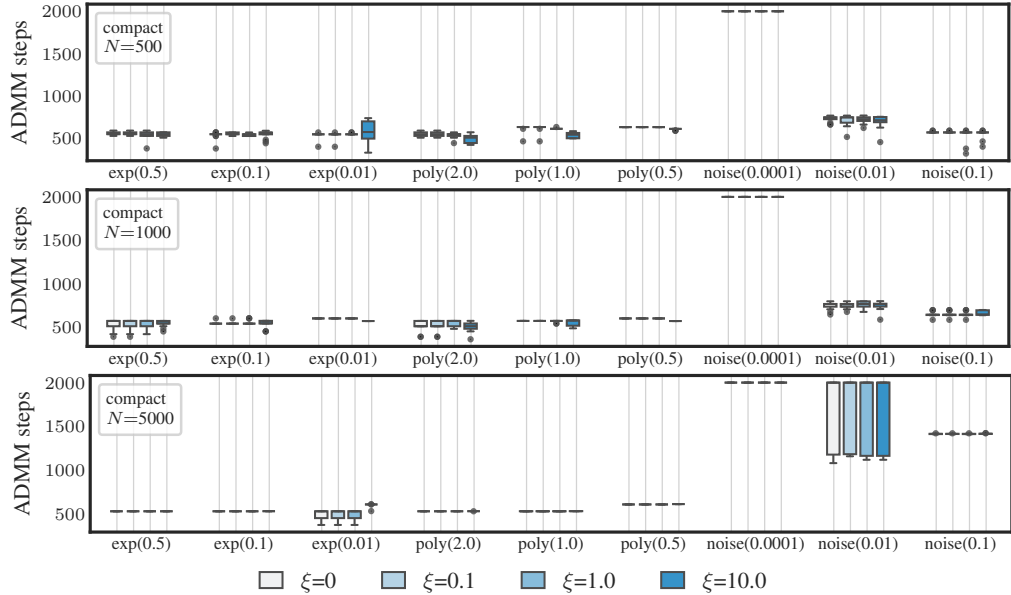


Figure 12: **Number of ADMM iterations in SKETCHLORD**, for different matrix types and sizes. See Section A.5 and Figure 13 for further discussion.

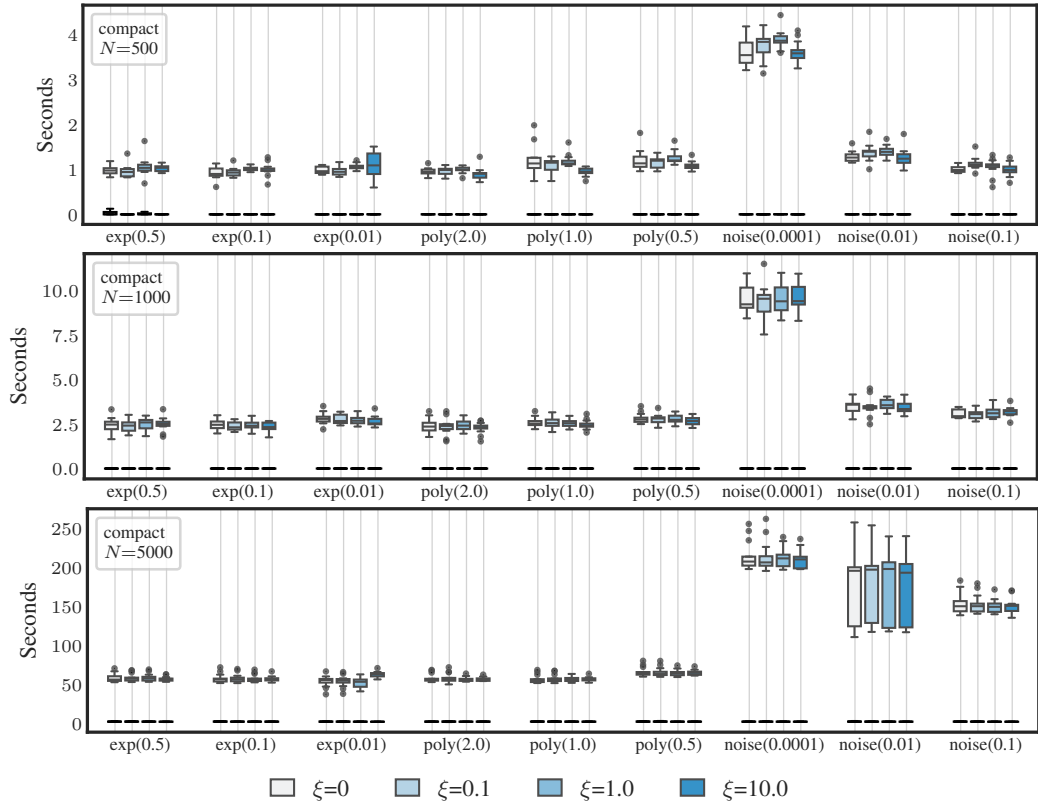


Figure 13: **Runtimes of SKETCHLORD vs. SSVD:** Total elapsed time, in seconds, for different matrix sizes and values of ξ . The thin boxes in the near-zero mark correspond to the SSVD runtimes, and the boxes above to SKETCHLORD. Note how the overhead of SKETCHLORD is mostly determined by the number of ADMM iterations (Alg. 1 and Figure 12).